UCID-17037

Lawrence Livermore Laboratory

STATUS OF 2XIIB PLASMA CONFINEMENT EXPERIMENTS

F. H. Coensgen, J. F. Clauser, D. L. Correll, W. F. Cummins, C. Gormezano, B. G. Logan, A. W. Molvik, W. E. Nexsen, T. C. Simonen, B. W. Stallard, and W. C. Turner

February 11, 1976

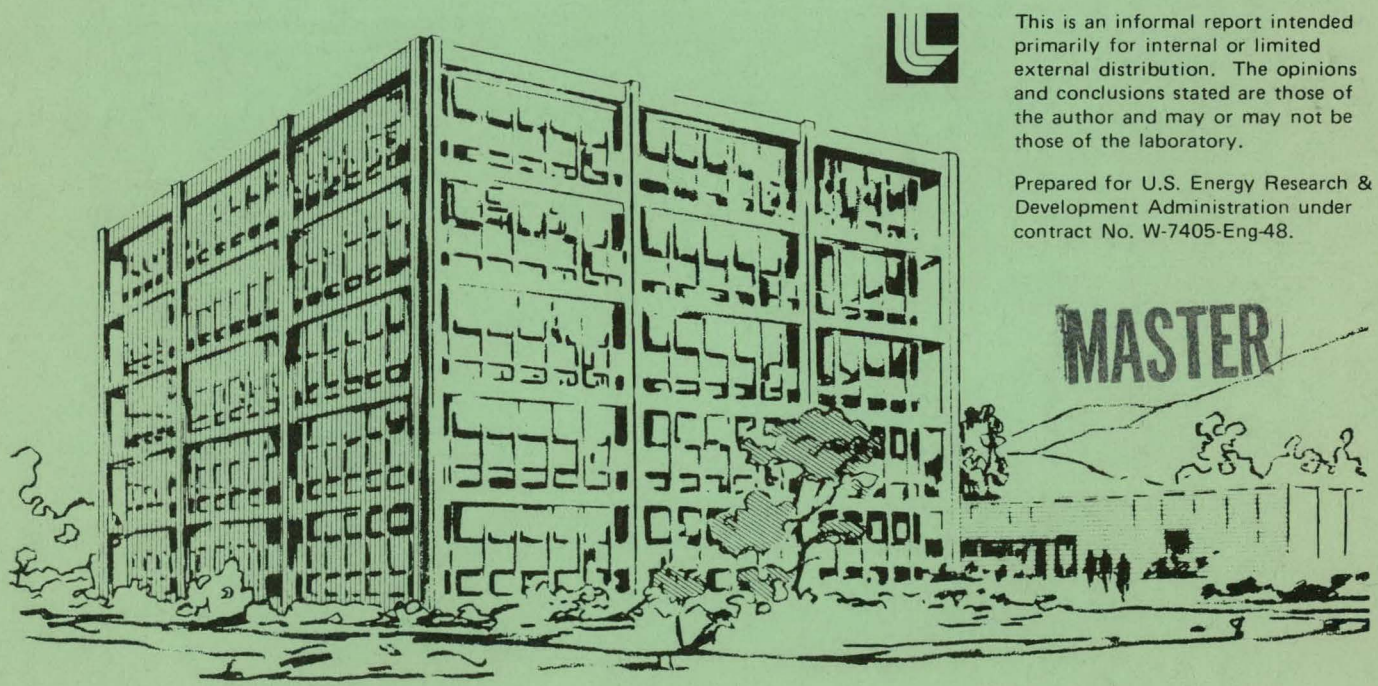

This is an informal report intended primarily for internal or limited external distribution. The opinions and conclusions stated are those of the author and may or may not be those of the laboratory.

Prepared for U.S. Energy Research & Development Administration under contract No. W-7405-Eng-48.

MASTER

DISTRIBUTION OF THIS DOCUMENT IS UNLIMITED

DISCLAIMER

This report was prepared as an account of work sponsored by an agency of the United States Government. Neither the United States Government nor any agency Thereof, nor any of their employees, makes any warranty, express or implied, or assumes any legal liability or responsibility for the accuracy, completeness, or usefulness of any information, apparatus, product, or process disclosed, or represents that its use would not infringe privately owned rights. Reference herein to any specific commercial product, process, or service by trade name, trademark, manufacturer, or otherwise does not necessarily constitute or imply its endorsement, recommendation, or favoring by the United States Government or any agency thereof. The views and opinions of authors expressed herein do not necessarily state or reflect those of the United States Government or any agency thereof.

DISCLAIMER

Portions of this document may be illegible in electronic image products. Images are produced from the best available original document.

NOTICE
This report was prepared as an account of work sponsored by the United States Government. Neither the United States nor the United States Energy Research and Development Administration, nor any of their employees, nor any of their contractors, subcontractors, or their employees, makes any warranty, express or implied, or assumes any legal liability or responsibility for the accuracy, completeness or usefulness of any information, apparatus, product or process disclosed, or represents that its use would not infringe privately owned rights.

CONTENTS

MASTER
DISTRIBUTION OF THIS DOCUMENT IS UNLIMITED

STATUS OF 2XIIB PLASMA CONFINEMENT EXPERIMENTS

ABSTRACT

This report describes the status of 2XIIB neutral beam injection experiments with stabilizing plasma. The stream suppresses ion-cyclotron fluctuations and permits density buildup to 5×10^{13} cm^{-3}. The ion energy is 13 keV, and electron temperature reaches 140 eV. Plasma confinement increases with ion energy and $n\tau$ reaches 7×10^{10} $cm^{-3} \cdot s$ at 13 keV. The $n\tau$ energy scaling is consistent with electron drag and ion-ion scattering losses. Buildup on a streaming plasma in a steady-state magnetic field is described.

INTRODUCTION

The primary objective of the 2XIIB experiment is to investigate scaling of $n\tau$ at higher ion energies than could be obtained in 2XII. A second objective is the use of neutral beam injection to sustain the plasma density. These objectives are central elements in mirror reactor concepts.

The 2XII plasma was known to form a suitable target plasma.[1] To insure that definitive experiments could be conducted even if plasma lifetimes did not increase with higher ion energy, a neutral beam injection system was built that could ultimately deliver sufficient current to sustain plasma loss rates as rapid as those in 2XII. There were two principal areas of concern about the prospects of success of the 2XIIB experiment; microinstabilities and vacuum conditions. During the first 6 months of 2XIIB operation, these two problems prevented us from achieving our objectives. Then, with the use

of a stabilizing plasma stream and minor vacuum system improvements we obtained the results described in this report.

It had been predicted[2,3] that ion-cyclotron microinstabilities would limit particle confinement in mirror experiments to a few tens of microseconds. Several sources of free energy were identified that could drive ion-cyclotron instabilities: velocity-space mirror loss cone, radial-density gradient, and narrow velocity and/or angular distribution of particles.

Although an ion-cyclotron instability with the characteristics of the drift loss-cone mode had been observed in 2XII,[4] lifetimes exceeded 200 μs. There also were quiescent modes of machine operation with even longer lifetimes and very weak ion-cyclotron oscillations. However, even in the best confinement runs, loss rates exceeded the classical Coulomb rate.

It was thus not possible to predict plasma containment in 2XIIB. Several facts were clear however. With higher ion energy, achieved by beam injection, 2XIIB would have a steeper radial-density gradient (measured in gyroradii), and a narrower angular-distribution function in velocity and angle. With a higher electron temperature, 2XIIB would have a larger velocity-space ambipolar hole. These features increase the free-energy reservoir that can drive microinstabilities. On the other hand, the shorter axial length of 2XIIB (measured in gyroradii) reduces the amplification factor of the convective loss-cone mode[5] and insures the stability of negative-energy modes.[6]

Initial experiments demonstrated that the ion-cyclotron fluctuation amplitude increased with neutral beam injection, and the density could not be sustained. Spreading the ion energy distribution by programming the beams at different energies had little effect. The instability did not cause angular spreading, suggesting that $k_{\parallel} \ll k_{\perp}$.

Following a theoretical suggestion by Post[7] and experiment indications from PR6,[8] PR7,[9] and 2XII, we injected a plasma stream along magnetic field lines. A priori, it was not obvious that a stream with unknown plasma characteristics would provide stability because theory required a rather specific stream density and temperature. In fact, we find that the stream does not provide complete stability. Rather, we believe that a low fluctuation level that persists with stream injection adjusts the stream and hot-ion distribution functions, by turbulent diffusion, to maintain a marginally stable state.[10]

The reduced fluctuation level permitted the plasma density to build up with neutral beam injection.[11] In July 1975, the following parameters were attained:

- Mean ion energy to 13 keV,
- Central densities to 4×10^{13} cm^{-3},
- Central plasma betas of 0.4, and
- Particle lifetimes increasing with ion energy and reaching $n\tau = 7 \times 10^{10}$ cm^{-3}·s at 13 keV.

Since July, we have reconfirmed these results with additional measurements and have been able to reach 25% higher density and beta.

This report summarizes the present status of 2XIIB experiments and discusses several topics that have recently been investigated. These include measurements of electron temperature,[12] plasma density profiles,[13] fluctuation spectral properties,[14] direct observations of turbulent diffusion, ion energy scaling, and measurements of the plasma stream. We also describe experiments with 5-ms duration that show no significant differences in plasma behavior compared to shorter experiments but that do show the effects of vacuum degradation.

Perhaps our most important new result is the demonstration that the stabilizing plasma stream provides a suitable target plasma in a steady-state mirror field. The plasma state reached with beam injection with the stream is identical to that obtained with a target plasma trapped with pulsed magnets. Thus, for the first time, a startup method for a dc mirror system has been demonstrated.

THE 2XIIB EXPERIMENTAL FACILITY

This section briefly describes the hardware associated with the 2XIIB plasma confinement experiment. The four principal components of 2XIIB are the pulsed magnet set,[15] the high-vacuum chamber,[16] the neutral beam injection system,[17] and the plasma diagnostics. The 2XIIB device is shown in Fig. 1, while the plasma diagnostics are shown in Fig. 2.

The magnet set consists of dc guide coils, trapping gate magnets, and a Yin-Yang compression magnet. This minimum-B magnet set provides a central field of 0.67 T and a 2:1 mirror ratio. The 57,000-litre vacuum system consists of a nonmetallic central Pyroceram* vacuum chamber, two end tanks for pumping plasma end losses, and two large source tanks for pumping gas from the neutral beam injectors. The neutral beam injection system employs a total of twelve 50-A, 20-keV Lawrence Berkeley Laboratory (LBL) injector modules, six on each side of the machine. Plasma diagnostics used on 2XIIB are in most part similar to those used elsewhere. The neutral beams are also used for diagnostic purposes.

*Reference to a company or product name does not imply approval or recommendation of the product by the University of California or the U.S. Energy Research and Development Administration to the exclusion of others that may be suitable.

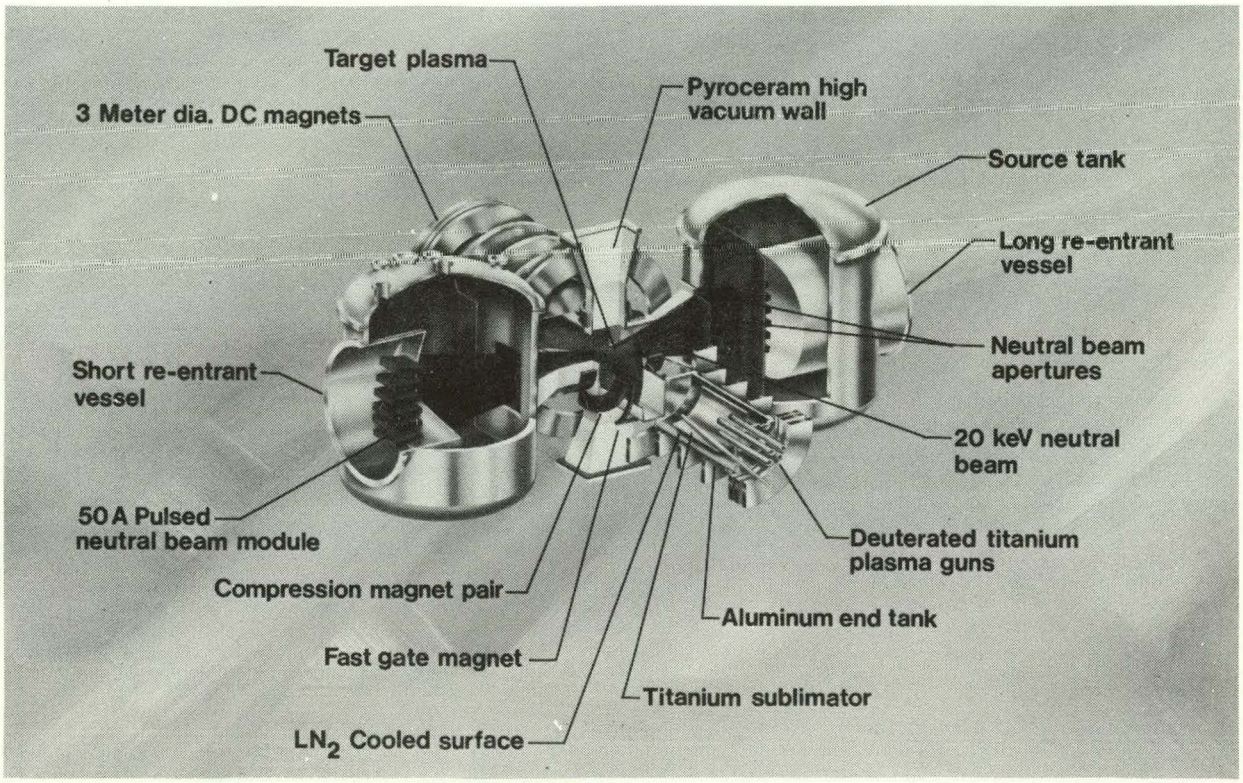

Fig. 1. The 2XIIB device.

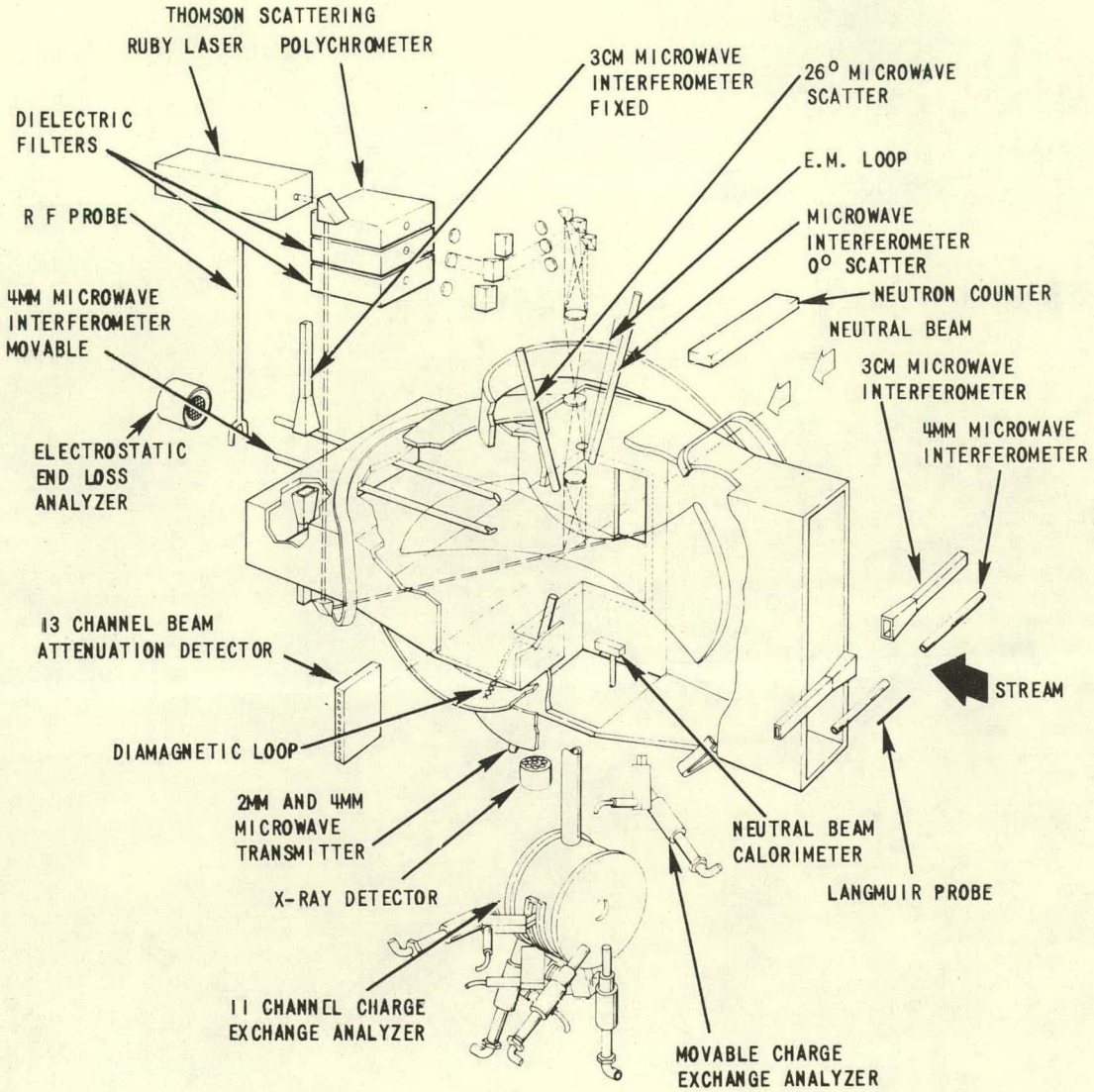

Fig. 2. 2XIIB plasma diagnostics.

Magnet System

The trapping and compression magnet sets are energized with capacitive energy-storage systems. The dc solenoids are powered by rectifier power supplies.

The pulsed magnets are fabricated from 20-mm^2 water-cooled copper conductor. The compression coils are wound in a 2-1/2 turn, 4-filar pattern. The low-inductance fast gate is wound as a 1/4-turn coil and the slow gate as a single-turn coil. To withstand large forces on the windings, the entire pulsed magnet is imbedded in a glass-reinforced epoxy structure.

The fast gate rise time is 15 μs and that of the compression coil is 500 μs. The compression coil is crowbarred at peak current, and the current then decays with a 10-ms e-folding time constant. The compression coils are normally operated at 800 kA-turns to produce a pulsed central field of 0.47 T. The dc coils normally operate at 0.2-T guide field, providing a total central field equal to 0.67 T.

A plot of magnetic field lines at the end of compression is shown in Fig. 3. The mirror ratio is 2:1. In the longitudinal direction, the magnetic field strength can be approximated by the parabola

$$B(z)/B_0 = 1 + (z/75)^2, \tag{1}$$

where z is in cm. In the radial direction, the magnetic field strength is approximately

$$B(r)/B_0 = 1 + (r/55)^2, \tag{2}$$

where r is in cm.

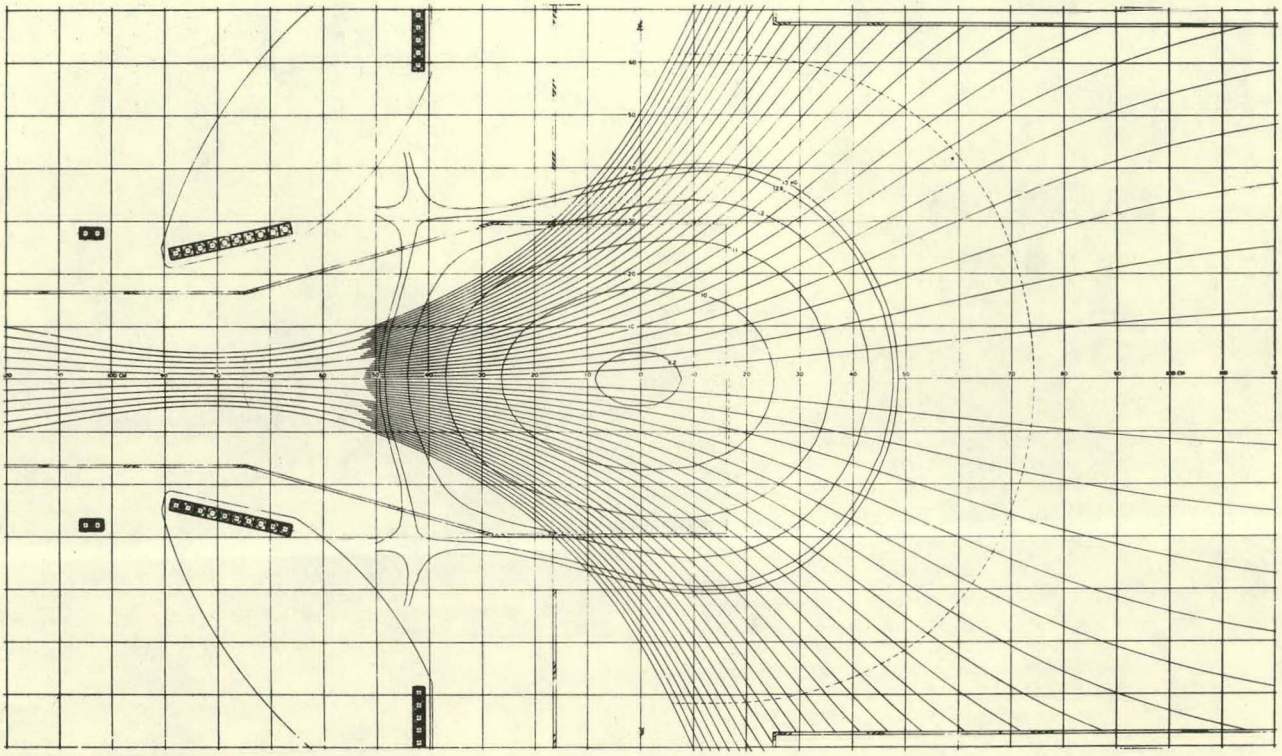

Fig. 3. 2XIIB magnetic field line plot.

High-Vacuum Chamber

The high-vacuum chamber surrounding the plasma confinement region fits inside the pulsed magnet and has a unique design. To avoid distorting the pulsed magnetic field, it is nonmetallic. A guard vacuum (approximately 10^{-5} Torr) separates the high-vacuum chamber wall from atmospheric pressure. The high-vacuum side is fabricated out of Pyroceram panels joined with RTV silicone rubber and supported on the guard-vacuum side by a glass-reinforced epoxy structure. A second set of Pyroceram liners shields the RTV seams from plasma bombardment and provides a surface for titanium deposition. Before each shot, a fresh surface at least several monolayers thick is deposited on all the high-vacuum chamber walls.

Neutral Beam System

The 2XIIB neutral beam system was designed with an equivalent current capability of 600 A D^0 atoms at 20 keV to insure that a hot, dense plasma could be sustained with no improvement in plasma confinement compared to 2XII. Since an order of magnitude improvement in plasma confinement was achieved at the higher ion energy of 2XIIB, full current output is not required for our present experiments.

The characteristics of the 50-A, 20-keV LBL modules are described in the literature.[18,19] Of particular concern for 2XIIB is the pumping of gas from the injector. The neutral gas load in equivalent atom current is shown schematically in Fig. 4. The thermal gas is pumped primarily by two titanium-gettered expansion chambers, separated from each other and from the plasma region by baffles with apertures just large enough to pass the energetic neutrals. These expansion chambers presently keep the gas pressure from the neutral beam injectors sufficiently low in the plasma containment

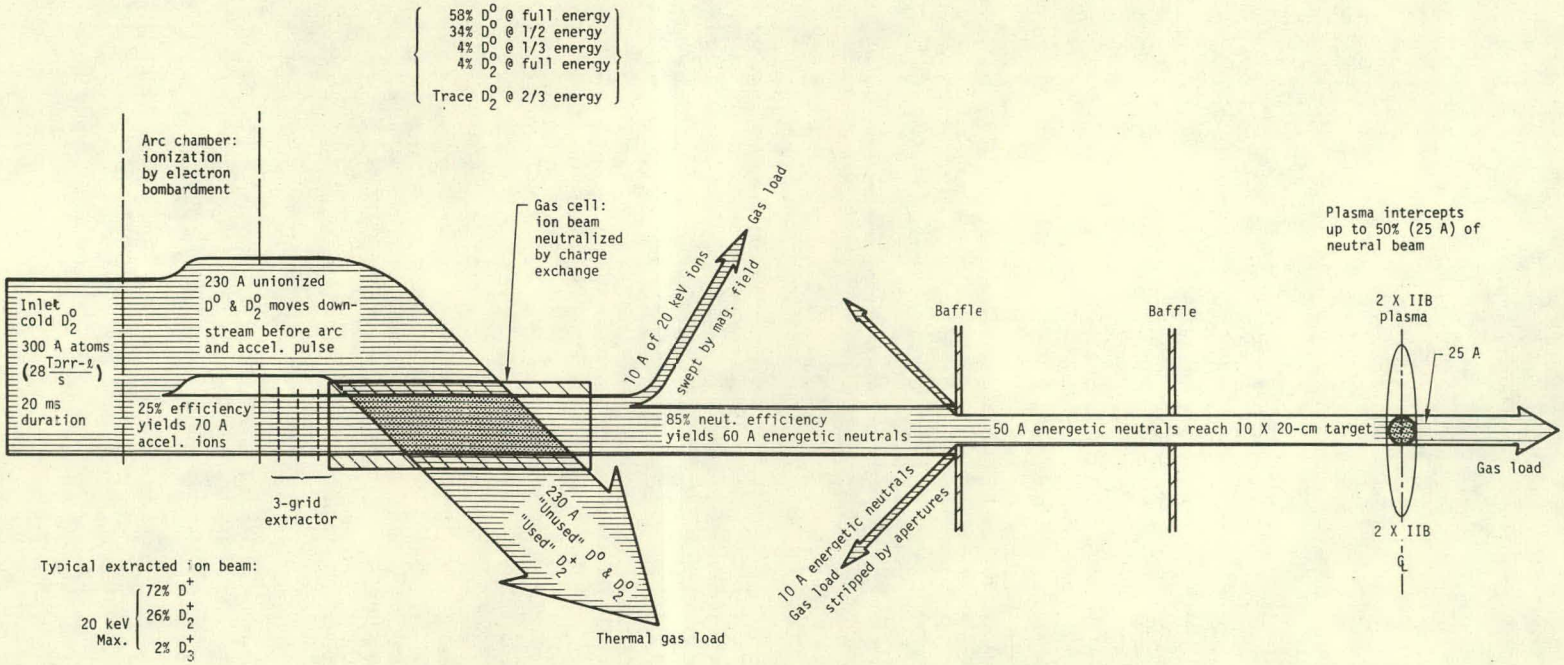

Fig. 4. Schematic of neutral beam injection system gas handling.

region for about 5 ms. Although 5 ms is adequate for present experiments, liquid nitrogen-cooled titanium surfaces will be used to extend this duration for future experiments.

Plasma Diagnostics

2XIIB plasma diagnostics are shown in Fig. 2. Density is measured with seven microwave interferometers, a four-position Thomson scattering system, 13 channels of neutral beam attenuation,[20] and a crossed-beam system employing an absolutely calibrated, 11-channel, charge-exchange analyzer and the neutral beams.[21] Ion energy is measured with the 11-channel charge-exchange analyzer and a single-channel movable analyzer. Additional measurements of ion energy are obtained from a diamagnetic loop and from a neutron detector. Electron temperature is measured by Thomson scatter. Microinstabilities are detected by high-impedance electrostatic probes and with microwave beams.[22] An electrostatic end-loss analyzer measures the end-loss current and energy distribution. In addition, we monitor x-ray,[23] H_α, and total light emissions. Plasma-stream characteristics are measured with microwave interferometers, movable Langmuir probes, the end-loss analyzer, and with several of the diagnostics listed above.

PLASMA CONFINEMENT EXPERIMENTS

This section describes experimental results on stream-stabilized plasma with neutral beam injection. We describe

- The effect of the plasma stream on the confined plasma,
- Measurements that indicate that the bulk of the plasma ions are hot,

- Measurements of plasma radial and axial density profiles, and
- Measurements of ion-cyclotron fluctuation characteristics.

Stabilization by Streaming Plasma

The effect of stream stabilization on plasma parameters is discussed in this section. The main effect of the plasma stream is to reduce plasma losses by suppressing ion-cyclotron fluctuations and allowing the density to buildup. The stream also reduces the electron temperature. The reduced electron temperature and fluctuation amplitude act together to lower the mean ion energy. All of these effects are illustrated in Fig. 5.

The data in Fig. 5 were derived from two series of shots, one without streaming plasma and the other with streaming plasma. Electron temperature vs time measurements were made by changing the firing time of the Thomson scattering laser. All of the shots in Fig. 5 were taken with a plasma target trapped at 0.6 ms and heated by magnetic compression. In all cases, the neutral beams were fired at the peak of compression 1.1 ms. With the plasma stream, the neutral beam current and duration were 200 A and 1.6 ms; and without plasma stream, 200 A and 1.2 ms, respectively.

Figure 5(a) shows central plasma electron density vs time. These data were obtained simply by dividing 2-mm microwave interferometer measurements of line density by a mean plasma diameter equal to 14 cm. This diameter is based on radial profile data described later (see p. 9). With and without streaming plasma, the plasma target densities are comparable. With no stream, the neutral beam maintains the density at 1.8×10^{13} cm^{-3} for a brief 0.3-ms period. After this, the beam buildup rate cannot keep up with the plasma losses due to the increasing amplitude of ion-cyclotron fluctuations.

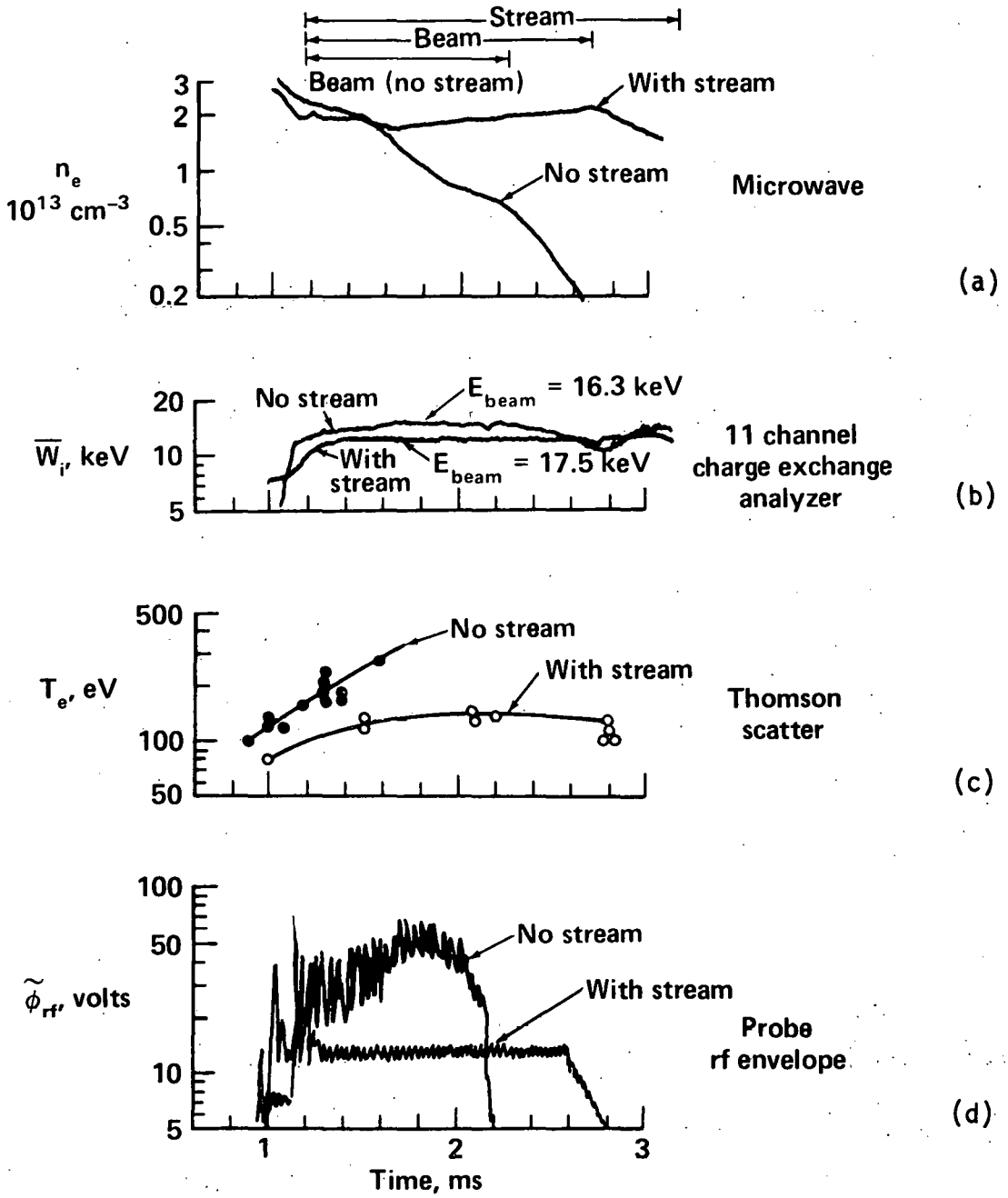

Fig. 5. The effect of plasma stream on (a) electron density, (b) mean ion energy, (c) electron temperature, and (d) ion-cyclotron fluctuation amplitude.

By contrast, the density with a plasma stream continues to build up until the neutral beams are shut off.

The mean deuteron ion energy is shown in Fig. 5(b). Without the stream, the mean ion energy increases rapidly. With streaming plasma, the mean ion energy rises more slowly to 12 keV within 0.3 ms of beam turn-on. This is comparable to but less than the time required for neutral beams to replace the target plasma by charge exchange. In spite of the fact that the beam energy is higher with the stream (17.5 keV) than without (16.3 keV), the mean ion energy is lower. This reduced ion energy results from lower fluctuation levels and increased ion cooling by low-energy electrons, as illustrated in Fig. 5(c) and 5(d).

In Fig. 5(c), the electron temperature with no stream rises rapidly to 250 eV, at which point the density falls too low for reliable Thomson scattering measurements. With the stream, the electron temperature increases from 75 eV to about 140 eV in 0.5 ms, and then stays relatively constant.

Figure 5(d) illustrates that the stream lowers the ion-cyclotron fluctuation amplitude by a factor of 2 to 4. The rf amplitude in this series of shots is higher than in most of our operation with higher streaming-plasma input. The large decrease in fluctuation amplitude at 2.2 ms with no stream occurs when the hot-plasma density drops to a low enough level that the plasma is stabilized by background cold gas, much the same as in 2XII partially gettered operation.

Evidence that Ions are Hot

Among the first questions considered with stream buildup was whether the rise in electron density in Fig. 5(a) or Fig. 6(a) results from increase in

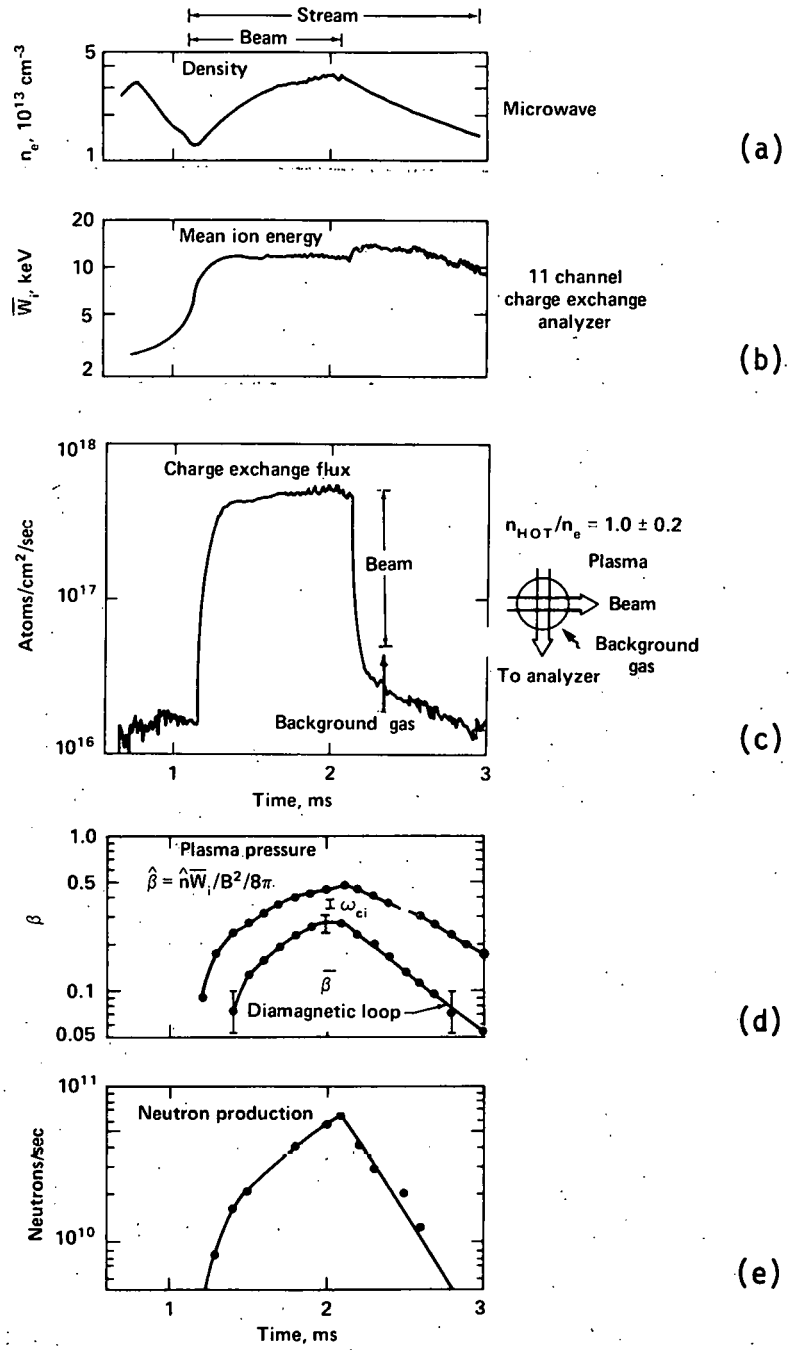

Fig. 6. Evidence that ions are hot. Measurements of (a) electron density, (b) mean ion energy, (c) charge exchange flux, (d) plasma beta, and (e) neutron production.

hot-ion or cold-ion density.[20] Although the average energy of charge-exchange flux shown in Fig. 6(b) indicates that the mean ion energy has increased, it is possible that the hot atoms detected are representative only of the tail of an ion distribution with much lower mean energy. This possibility is ruled out by absolute measurements of fast-atom charge-exchange flux, plasma diamagnetism, frequency shift of ion-cyclotron fluctuations, and absolute measurements of neutron production.

The first direct measurement of the fraction of hot ions is indicated in Fig. 6(c). By switching the neutral beams off, we determine that the charge-exchange flux consists of a component due to charge exchange off the beam and a smaller contribution due to background gas. The beam component originates at the center of the plasma where the analyzer acceptance cone intersects the neutral beam cross section. The key point of this measurement is that only particles above 500 eV are detected by the analyzer; cold ions are not detected. The change in analyzer signal when the beams are switched off is therefore proportional to the product of (1) hot-ion density, (2) ion angular distribution, (3) neutral beam atom density, (4) charge-exchange reaction rate, and (5) analyzer sensitivity. Since all factors except density are known, the beam component of charge-exchange flux provides a measure of the hot-ion density. This measurement of hot-ion density is within 20% of the electron density. The discrepancy is within the uncertainty of the absolute calibration of the fast-atom analyzer. We therefore conclude that the bulk of the plasma ions are hot.

A second indication of a hot-plasma density is obtained from diamagnetic loop measurements shown in Fig. 6(d). The diamagnetic loop measures the plasma parameter $\overline{\beta}$, equal to the ratio of plasma energy density to vacuum magnetic field energy density, averaged over a 2.5-litre plasma volume. The

maximum value of beta at the plasma center, $\hat{\beta}$, shown in Fig. 6(d) is calculated from the central electron density and mean ion energy.

A third indication of high beta is a shift of the fluctuation frequency. Assuming this frequency is the ion-cyclotron frequency, we calculate the plasma beta from the expression

$$\beta = 1 - [\omega(\beta)/\omega(\beta = 0)]^2. \tag{3}$$

This value of beta shown in Fig. 6(d) lies between the maximum beta and average beta measured by the diamagnetic loop.

The fourth indication that the bulk of the plasma is hot is obtained from a comparison between measured and calculated neutron production rates. Figure 6(e) shows that the neutron production rate increases with an n^2 dependence. The measured rate for the shot shown in Fig. 6(e) reaches 6.5×10^{10} neutrons/s, whereas the calculated rate is 1.1×10^{11}. This 40% discrepancy is within the accuracy of the calculation, which is limited by lack of detailed knowledge of the high-energy tail of the ion distribution function and uncertainty due to spatial averaging over the plasma density profile.

Measurements of Plasma Density Profiles

Measurements of plasma density profiles are necessary to determine plasma volume, to determine radial and longitudinal density scale lengths, to interpret microwave line-density measurements, and to calculate the ion pitch-angle distribution. Horizontal and vertical density profiles at the plasma midplane (x and y in Fig. 7) provide a measure of azimuthal symmetry. The nonsymmetric axial profile due to the stream has been measured by injecting a stream from both ends, with diagnostics in one end.

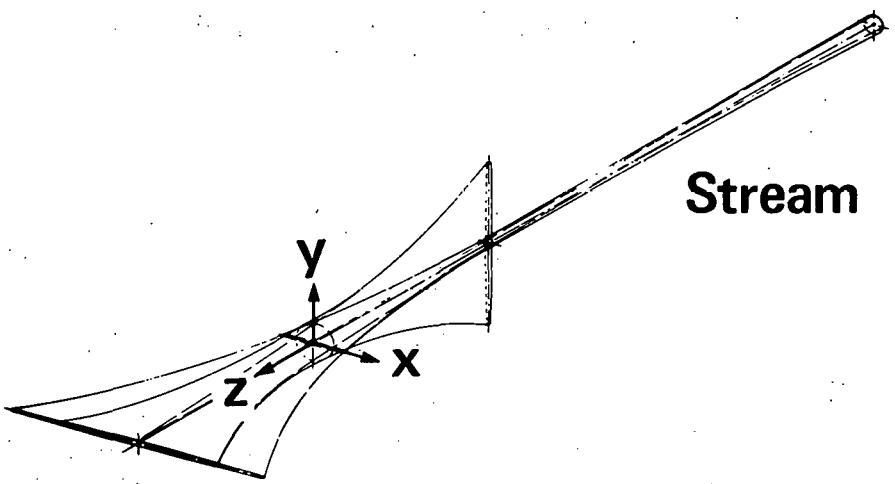

Fig. 7. Coordinate system for density profile measurements.

Density profiles in the horizontal plane are obtained from Thomson scattering measurements of electron density, microwave interferometer measurements of electron density along two chords, and radial scans of a collimated fast-atom detector that measures ion density profiles. The vertical profile is measured with a 13-channel neutral beam attenuation detector. Radial profile measurements in two orthogonal directions show that the plasma is azimuthally symmetric at $z = 0$ and that the mean plasma diameter is 13 to 14 cm. Since the gyroradius for a 14-keV deuteron is 3.5 cm, the plasma radial scale length varies from $R_p/a_i = 2$ at 14-keV mean ion energy to $R_p/a_i = 4$ at 3.5-keV mean ion energy.

Longitudinal density profiles are obtained with 2-mm and 4-mm microwave interferometers fixed at $z = 0$, a 4-mm interferometer movable from $z = 0$ to 130 cm, 4-mm and 3-cm interferometers at $z = 160$ cm, and a Langmuir probe at $z = 160$ cm. Axial density measurements indicate that the hot-ion distribution along z is determined by the injected neutral beam profile. This is expected since the characteristic time scale for charge-exchange replacement of the plasma ions with beam-injected atoms is short compared to classical ion-ion scattering times. The mean hot-plasma axial length (~ 40 cm) is therefore less than the distance between mirrors (150 cm), and the velocity-space distribution of ions is anisotropic (high-beta, axial pinching modifies this conclusion). The plasma density outside the mirrors that is the source of streaming plasma between the mirrors exceeds the central plasma density. The bulk of this exterior plasma is held out of the mirror confinement region. At the mirror, the streaming density is 20% of the central density between mirrors.

Horizontal Profile

Thomson scattering provides a direct measurement of plasma electron density at x = 0, 4, 6, and 8 cm. These data, shown in Fig. 8, indicate a radial plasma profile in agreement with that measured by other methods.

A 4-mm microwave interferometer on the plasma diameter and a second interferometer on a plasma chord at x = 7 cm provide an estimate of the mean plasma diameter. A parabolic profile

$$n(r)/n(0) = 1 - (r/10.6)^2, \tag{4}$$

shown in Fig. 8, is consistent with this microwave measurement and yields a mean plasma diameter

$$\bar{\ell} = n^{-1}(0) \int n d\ell \tag{5}$$

equal to 14 cm.

The above two measurements of electron density are compared with a measurement of 17-keV charge-exchange atoms in Fig. 8. These data are obtained with a movable detector that views the plasma with 3.5-cm resolution in the x-direction. The measured distribution has been shifted one gyroradius to obtain the guiding-center distribution of plasma ions shown in Fig. 8. These data have been normalized to the central density determined from the other methods. The hot-ion distribution can be fit by a Gaussian profile:

$$n(r)/n(0) = \exp\left[-(r/7.35)^2\right] . \tag{6}$$

This profile yields a 13-cm mean plasma diameter.

Vertical Profile

The density profile in the vertical (y) direction is measured with a 13-channel array of beam-attenuation detectors spaced on chords every 2 cm.

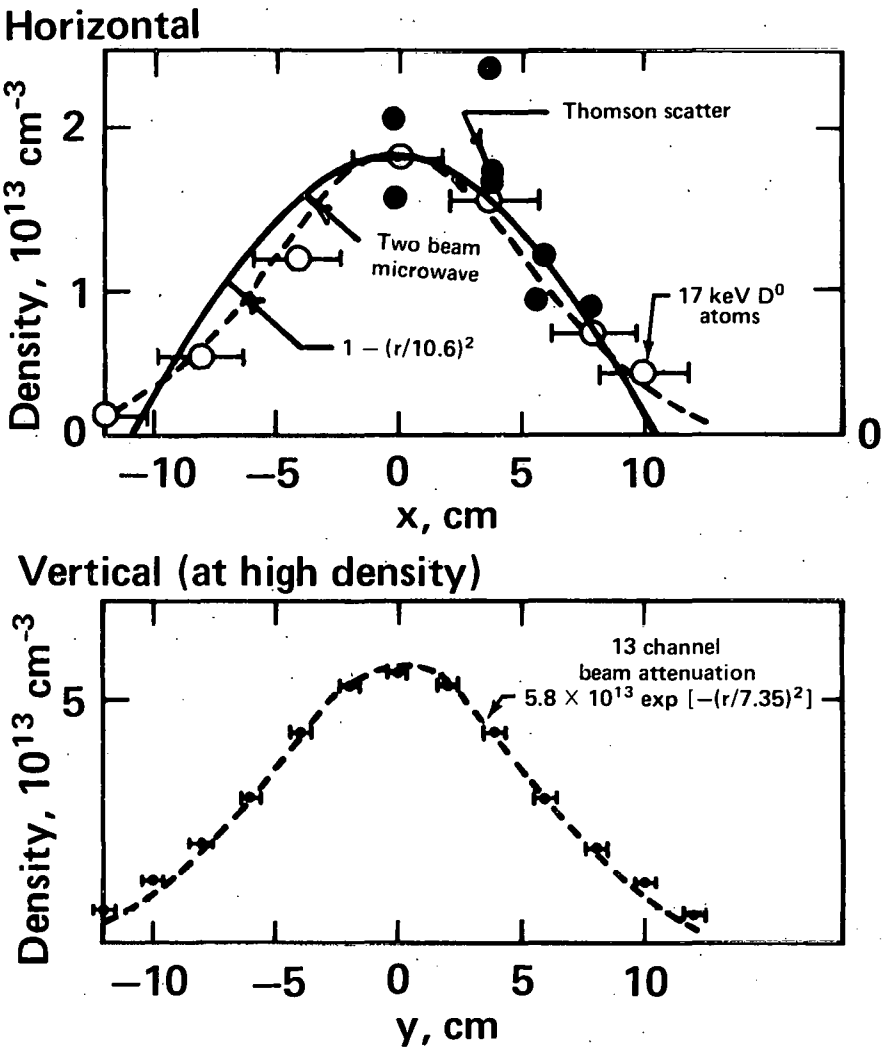

Fig. 8. Horizontal and vertical density profiles at midplane.

The detectors view one of the 12 neutral beams and have 8-mm resolution at the plasma. Beam attenuation is primarily by charge exchange and is 50% at a line density of 4.5×10^{14} cm^{-2} for typical 17-keV neutral beam extraction energy with 13-keV mean plasma ion energy. The measured line density data is Abel inverted to give the profile shown in Fig. 8. The curve is a least-squares fit of a Gaussian function to the measured data. The central density for this high-density shot is 5.8×10^{13} cm^{-3}. A central density of 4.8×10^{13} cm^{-3} is determined from the y-directed, 2-mm microwave line density using the measured beam-attenuation profile. This 20% discrepancy could result from asymmetry in the low-density wings of the radial profile, inaccuracies of atomic cross sections used to reduce the beam-attenuation data, and uncertainties of the fractions of full-, half-, and third-energy components of the neutral beam.

Axial-Density Profile

The axial-density profile is calculated from line-density measurements through the narrow dimension of the plasma fan. These measurements were made with a movable, 4-mm microwave interferometer. To determine the density profile, we assume the plasma cross section follows a magnetic flux surface (as in Fig. 3). The axial density profile is shown in Fig. 9. Whereas the data for $z > 0$ has been measured several times, the data for $z < 0$ has been measured only once. For comparison we show the "Holdren" collisional distribution that is considerably broader than the measured distribution. The measured distribution is primarily determined by the angular distribution of the injected neutral beams. On the streaming plasma gun side, the plasma density outside the mirror is higher than in the center. The mirror holds most of this density out, with only 5% of the external plasma able to penetrate to the mirror throat.

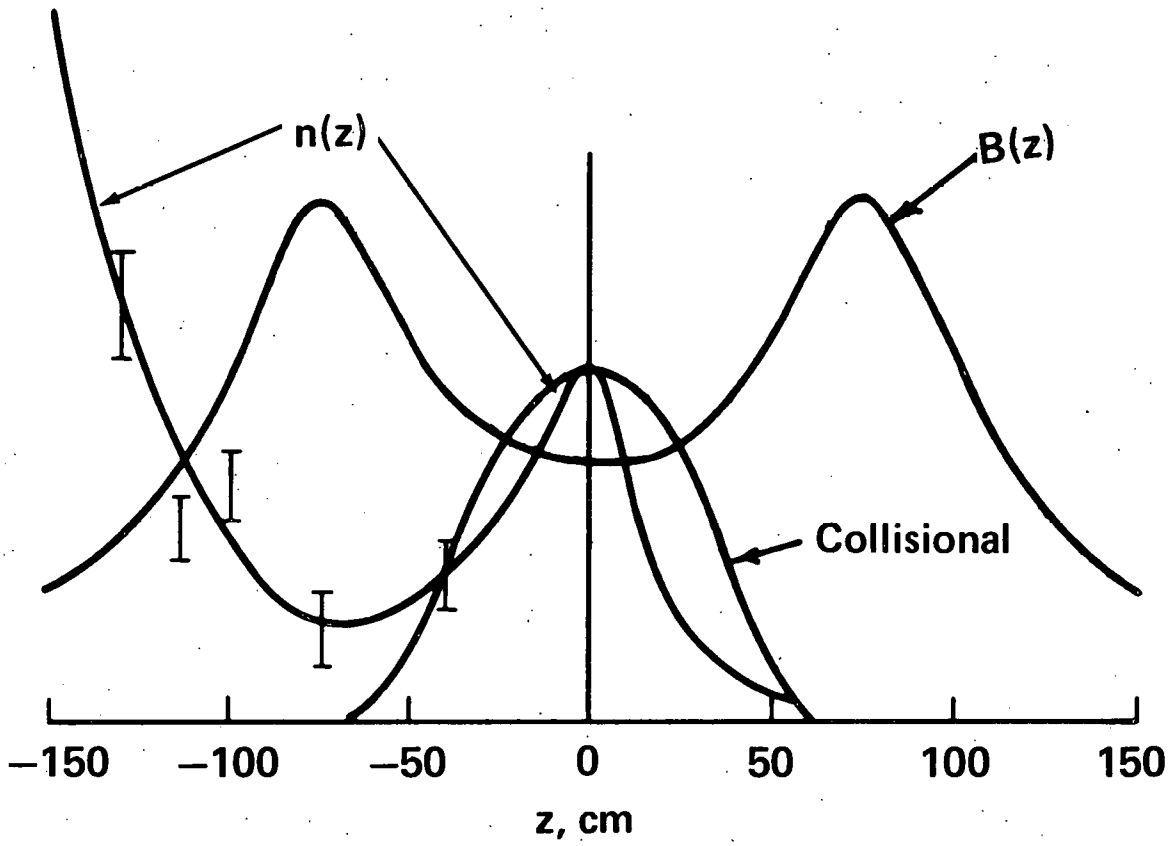

Fig. 9. Axial density profile.

Pitch-Angle Distribution

Axial measurements of plasma density can be used to calculate a pitch-angle distribution.[24] Figure 10 shows the midplane equilibrium angular distribution in terms of the variable $\mu = \cos\theta$. This distribution has been obtained using Hall's formula to invert an analytic fit to the data. Ignoring finite beta, the data is inverted using the vacuum magnetic field profile. To estimate the effect of finite beta, the vacuum magnetic field was depressed by the local beta determined from the measured axial-density profile.

Ion-Cyclotron Fluctuation Measurements

Ion-cyclotron fluctuations are detected with electrostatic probes located beyond the mirrors[4] and with microwave beams[25] at the center of the plasma as shown in Fig. 2. The probe has a 10-kΩ series resistance and detects floating potential oscillations. The probe frequency window extends from 0.1 to 20 MHz ($0.02 < \omega/\omega_{ci} < 4$), and oscillations as weak as 1-V peak-to-peak can be detected. A 4-mm microwave receiver detects phase modulation of a transmitted microwave beam. The phase modulation is caused by density oscillations within the plasma. This system is most sensitive to long-wavelength density perturbations. The minimum detectable signal corresponds to density oscillations of $\tilde{n}/n_0 \sim 10^{-3}$ for wavelengths in the range of $k_\perp a_i \sim 3$.

An example of the envelope of rf activity detected by the probe is shown in Fig. 11. During stream injection, the rf occurs in periodic bursts, whereas after the stream shuts off, the rf builds up to a higher level and is more continuous. This behavior is discussed in more detail below.

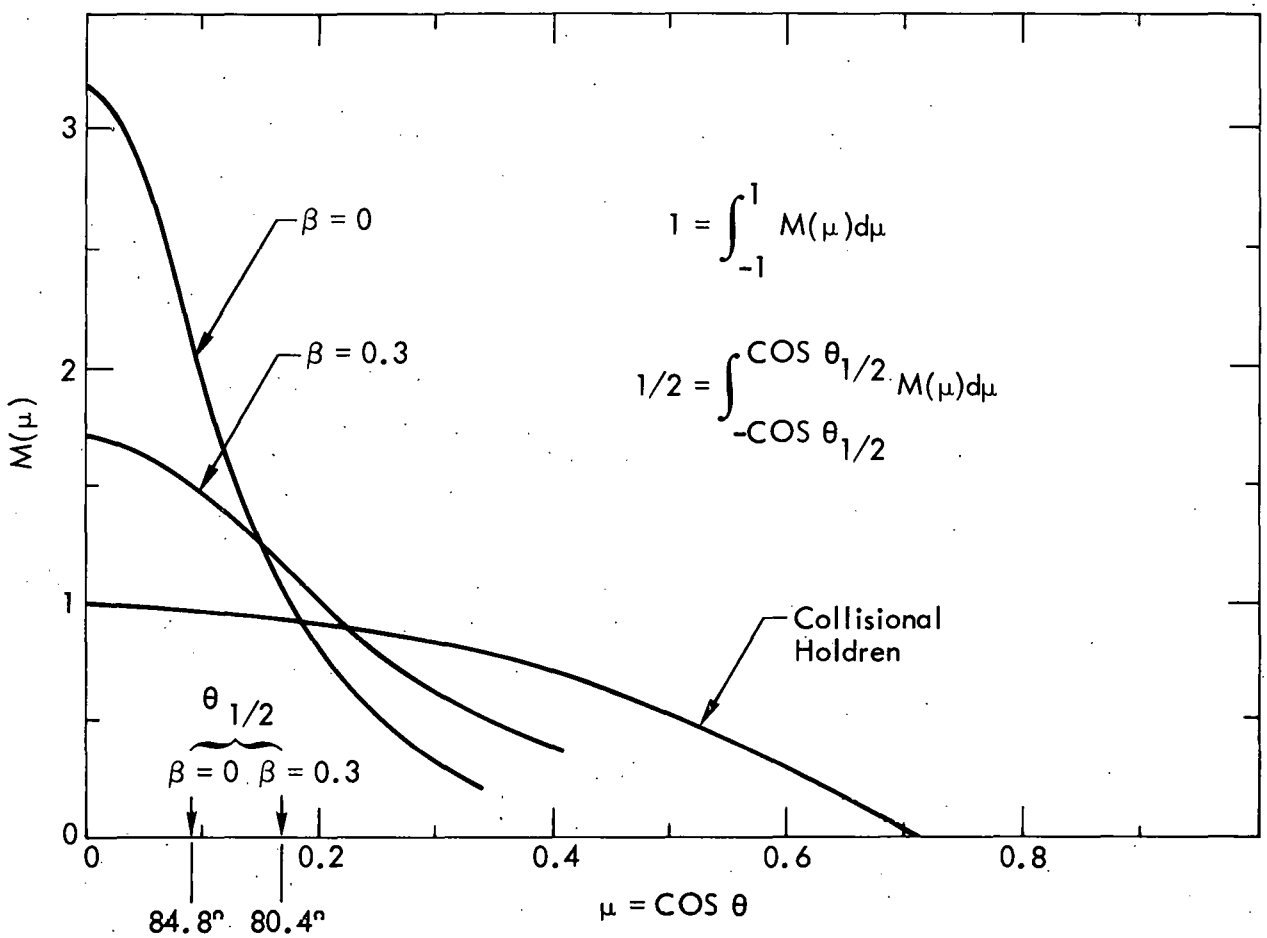

Fig. 10. Equilibrium ion angular distribution function.

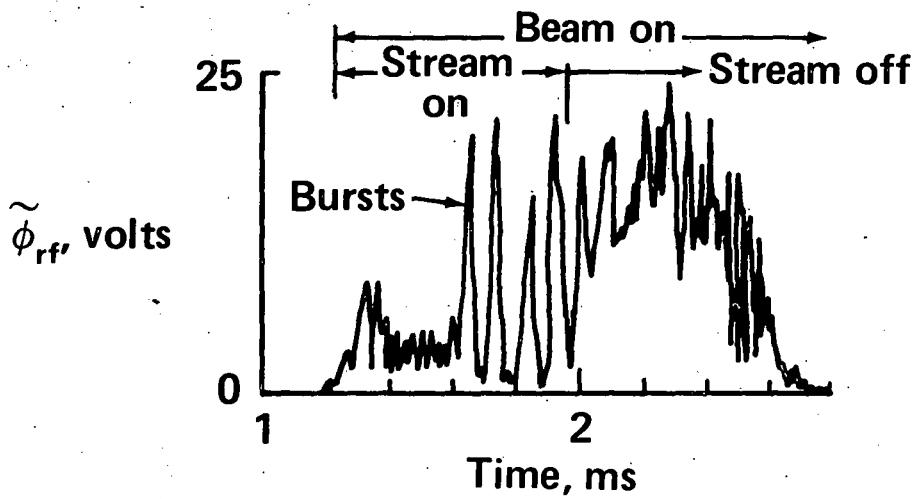

Fig. 11. Amplitude of ion-cyclotron fluctuation vs time.

Particle Loss Rate

The particle loss rate, shown in Fig. 12, increases linearly with the square of rf intensity. These data are all from the shot shown in Fig. 11. The key point made in Fig. 12 is that ion-cyclotron fluctuations, when not suppressed by the stream, cause rapid loss of plasma.

Frequency Spectra

The frequency spectra of the ion-cyclotron fluctuations detected by the rf probe are shown in Fig. 13. The two types of fluctuations referred to above, bursting with the stream on and continuous with the stream off, are characterized by their time behavior and spectral widths. The time-domain signals are recorded digitally with transient recorders. Fast Fourier transform techniques are used to compute power spectra.[22] The frequency spectra for both bursting and continuous noise are centered near ion-cyclotron frequency corrected for finite beta as indicated in Fig. 13. The bursting instability rises with a growth rate $\gamma/\omega_{ci} \sim 0.02$ and lasts ~ 70 ion-cyclotron periods.

Although the dominant frequency is the ion-cyclotron frequency, there are many instances when second and third harmonics are observed. Relative amplitudes of the fundamental and second and third harmonics are shown in Fig. 14 for such shots.

Wavelength Measurements

The wavelength of ion-cyclotron fluctuations is determined by combining measurements with the two tips of the rf probe displaced a distance L. The phase of the cross-amplitude spectrum[22]

$$P_{12}(\omega) = |P_{11}(\omega)\ P_{22}(\omega)|^{1/2}\ e^{ikL} \qquad (7)$$

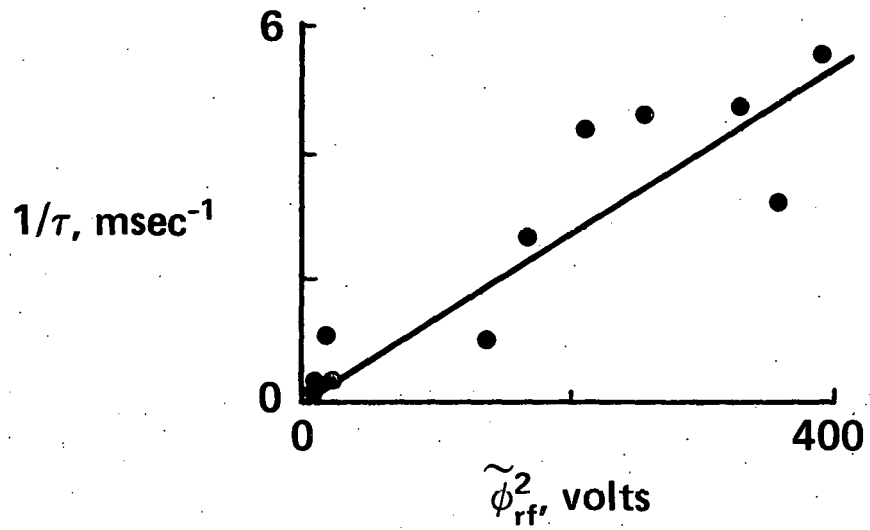

Fig. 12. Plasma loss rate vs ion-cyclotron fluctuation amplitude squared.

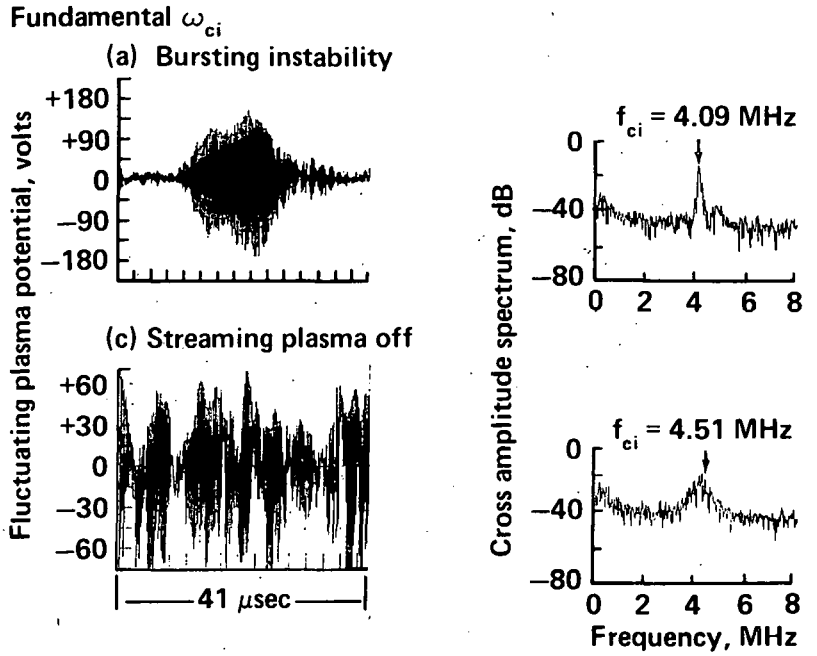

Fig. 13. Spectral properties of ion-cyclotron fluctuations.

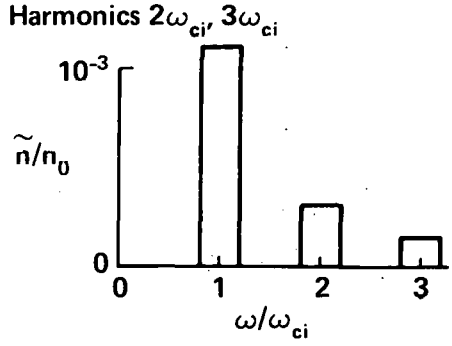

Fig. 14. Fluctuation spectrum with second and third ion-cyclotron frequency harmonics.

determines the oscillation wave number k. This is combined with the frequency measurement to calculate the magnitude and direction of the wave-phase velocity ω/k. Four wave-number measurements made during the bursts gave $k_\perp a_\perp$ from 2 to 5. The corresponding phase velocities range from 4.1×10^7 to 2.3×10^7 cm/s. In three of the four measurements, the wave-phase velocity was in the direction of the ion diamagnetic drift and in one case opposite. Two measurements of $k_\perp a_\perp$ after the stream shut off gave $k_\perp a_\perp = 3.7$ and $k_\perp a_\perp = 0.0$. In the first measurement, the wave-phase velocity was in the direction of the ion diamagnetic drift, and in the second, the phase velocity was indeterminate.

Ion Velocity-Space Diffusion Coefficient

A direct measurement of the increase in velocity-space ion diffusion when the stabilizing stream plasma is turned off is given in Fig. 15. The top three traces in Fig. 15 are 17-, 25-, and 39-keV deuteron charge-exchange fluxes measured perpendicular to the confining magnetic field. For comparison with the charge-exchange signals, the envelope of ion-cyclotron oscillations is shown at the bottom of Fig. 15. Although the peak amplitude of oscillation does not change appreciably when the streaming plasma turns off at 3.8 ms, there is a large buildup in the continuous level of oscillation.

When the streaming plasma is turned off, the 17-keV signal rapidly decreases. This is characteristic of all the charge-exchange signals below 17 keV that are not shown in Fig. 15 but lie in the bulk of the ion distribution function. By contrast, the 25- and 39-keV signals that are in the tail of the ion distribution after the stream turns off show a rapid

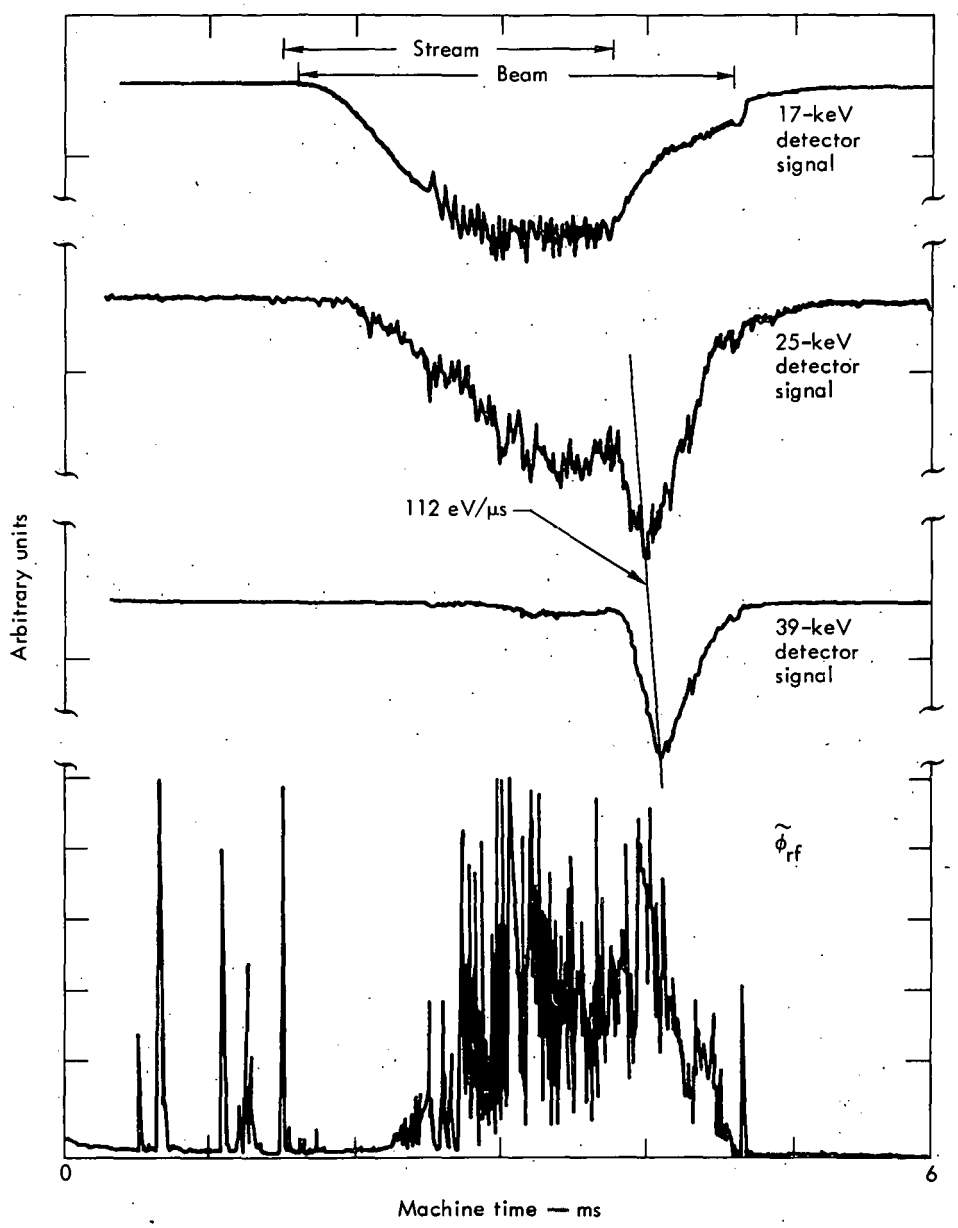

Fig. 15. Illustration of turbulent diffusion of ions to high energy.

increase. From the delay between the maximum signal heights in the 25- and 39-keV channels, we estimate an ion diffusion coefficient of 100 eV/μs.

Bursting

The spectral properties of the ion-cyclotron fluctuations accompanying bursting were described above. These bursts result in small decreases in the central line density (~ 5%) and larger decreases in the 90° charge-exchange flux (~ 20%), indicating a spread in angular distribution. This spread is confirmed by the movable microwave interferometer that detects an increase of particle density in the mirror regions during bursting, and by the end-loss analyzer that detects a large increase in the flux of ions above 1 keV. The density of the plasma is limited by the bursting when particles lost during the bursts equal particles trapped during the essentially loss-free quiet periods between bursts.

In the July experiments, bursting set in at a well defined density threshold of $\sim 3 \times 10^{13}$ cm^{-3} and plasma beta of 0.4. In later experiments, where more parameters have been varied, we find bursting at densities between 1 to 5×10^{13} cm^{-3} and at plasma betas as low as 0.1.

The repetition frequency of the bursts increases almost linearly with beam current. Since the buildup rate, in the absence of losses, is proportional to current, this variation implies that the fractional modulation of the density and 90° charge-exchange flux during the bursts is independent of the beam current strength, as is observed experimentally.

Re-aiming the beams to tangential injection at the machine center increased the repetition rate per unit current and decreased the percent modulation of the density and flux.

These observations suggest that the bursting is a relaxation phenomenon. One possible mechanism involves the ratio of stream to hot-plasma density. If stabilization of the plasma by the stream requires some minimum ratio of stream density to trapped plasma density, and the stream density is source limited, then it follows that the maximum trapped plasma density should be limited by the reappearance of the instability. Since the instability growth rate is fast compared with plasma buildup time, it appears unlikely that one can overshoot the stability limit of n_h/n_s and obtain relaxation oscillations. An alternative explanation involves the hypotheses that the increase in rf as the limit is approached reduces the stream density by rf plugging of the mirrors and drives the system more unstable. The instability eventually limits and dies out as ions turbulently diffuse into the loss cone. With the decrease of the rf, the stream density can once again penetrate the mirror and provide stability. The trapped plasma density at this time would be below the instability limit set by the normal stream density, and buildup would again occur until the limit was reached and the cycle repeated.

The evidence that the bursting in 2XIIB is due to this mechanism is as follows:

- In the case of plasma buildup on stream alone, the value of the final burst-limited density bears a direct relationship to the stream density.
- A sudden increase in stream density produced by firing a second stream gun after a bursting limit has been reached resulted in a rapid density increase to a burst-limited level almost double the previous value.

- End-loss measurements show that although the flux of energetic ions increases during the bursts, the current of lower-energy stream particles decreases, indicating a decreased penetration of the stream during bursts.

Characteristics of the Plasma Stream

In this section, we describe characteristics of the 2XIIB plasma stream, including measurements of the electrical gun characteristics, electron temperature, density profiles, and end-loss measurements. The locations of diagnostics used for these purposes are shown in Fig. 16. The streaming plasma gun is a standard deuterium-loaded, titanium-washer gun[26] driven by either a 20-kV, 2-Ω L-C pulse line or by a 3-kV, 0.2-Ω L-C pulse line.[27]

The picture which emerges from the measurements described below is that the streaming gun generates a 10^{14} density stagnant reservoir of plasma outside the mirror with an electron temperature of ~70 eV. Ions and electrons are contained for several transit times between the gun and the mirror. The stream density is attenuated in the mirror throat, allowing an electron temperature in the confinement region between mirrors to exceed that in the external plasma.

The current to the streaming plasma gun, the voltage at the gun, and the resulting electrical power are shown as functions of time in Fig. 17 for the 20-kV, 1-ms pulse line. The electrical input power is approximately 1 MW. with a 0.2-T guide field, approximately 0.3 MW of plasma power has been collected by a calorimeter on the other end of the machine, 7-m away. This streaming gun output power (mainly into electrons) is comparable to the power transfer to plasma electrons by hot ions slowing down.

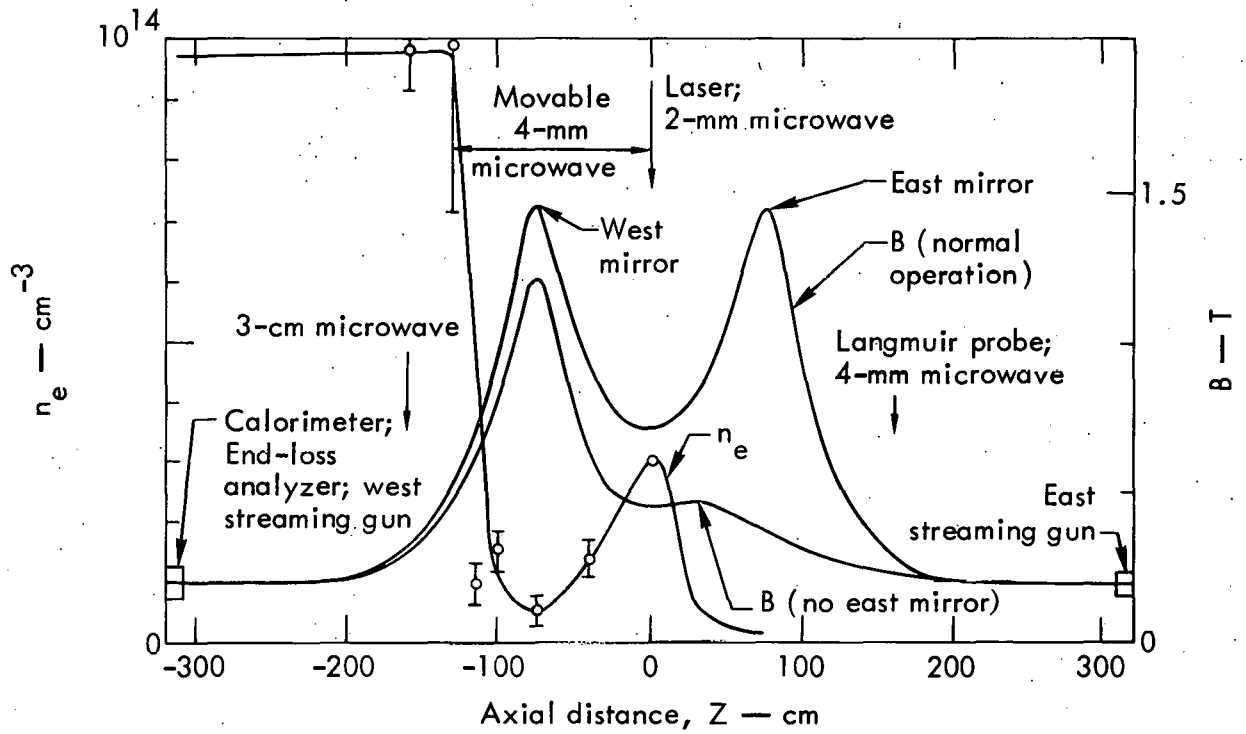

Fig. 16. Location of diagnostics used to study stream characteristics.

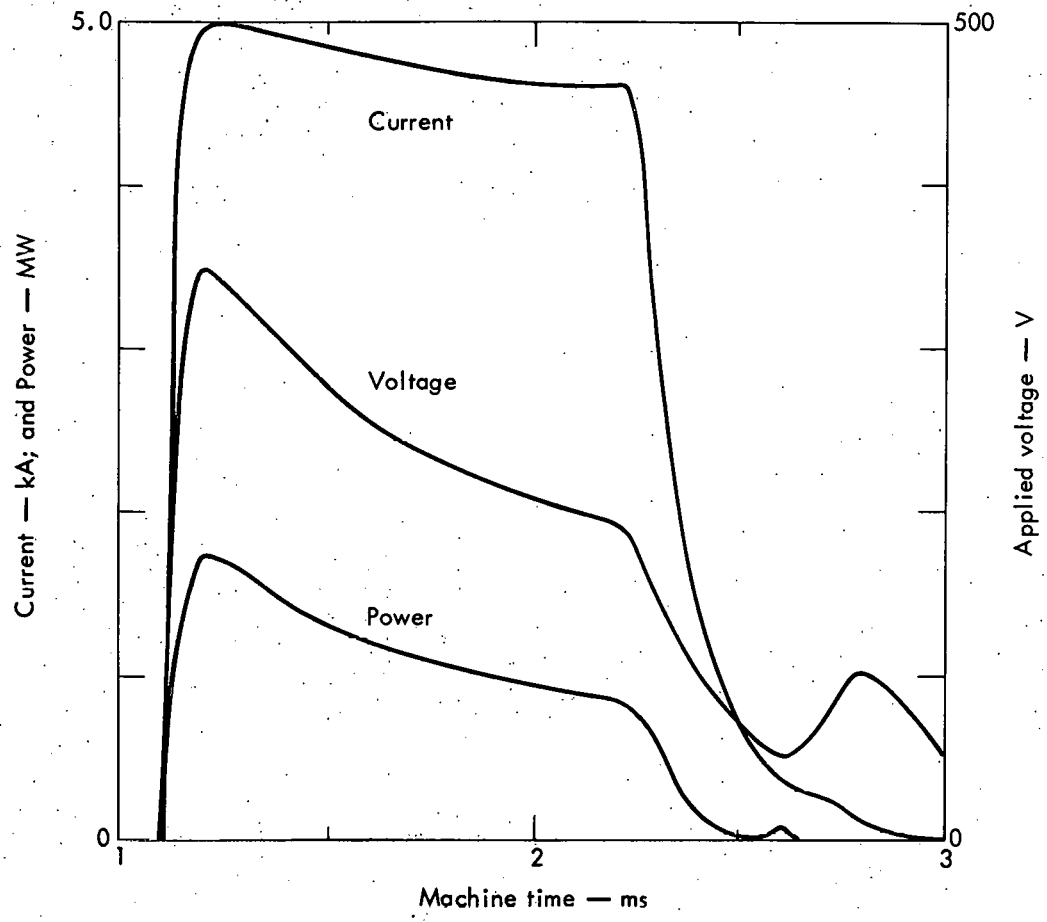

Fig. 17. Streaming-plasma gun current, power, and voltage vs time.

To determine if the gun alone could heat electrons, measurements were made with the streaming gun firing at the west mirror with the 0.2-T dc guide field. Thomson scattering measurements made between the gun and the mirror indicate a 70-eV electron temperature and a density of several times 10^{13} cm^{-3}. In the dc field alone, without the mirror, Langmuir probe measurements indicate a lower electron temperature and lower density, possibly due to poorer plasma containment. The density and electron temperature increase when a mirror is added, and increase still more when hot plasma is present. With hot plasma, the exterior ion containment time is estimated to be 25 ion sound speed transit times, and the exterior electron energy lifetime to be more than 30 electron transit times.

Langmuir probe ion saturation current radial profiles, made 150 cm from the streaming plasma gun with 0.2-T dc guide field, indicate that the streaming plasma has a 7.5-cm mean diameter. With compression coils and 0.2-T dc guide field, this 7.5-cm mean diameter maps into the shape shown in Fig. 18. Comparison of line density from an east streaming gun with a west streaming gun shows that the stream ellipticity exceeds 3.8.

The external plasma density is seen in Fig. 16 to decrease rapidly with the increasing magnetic field in the mirror region. The ions are presumably reflected by the mirror. Ion-cyclotron fluctuations (driven by the hot plasma) extending into the end region could aid reflection by "rf stoppering" ions at the external ion resonance zone.

The end-loss analyzer measures the total current through the mirrors (end loss plus streaming). Figure 19 shows this current as a function of time. The analyzer current sensitivity has been calculated rather than experimentally calibrated, and thus is subject to some uncertainty. The relative current-time dependence, which does not depend on this calibration,

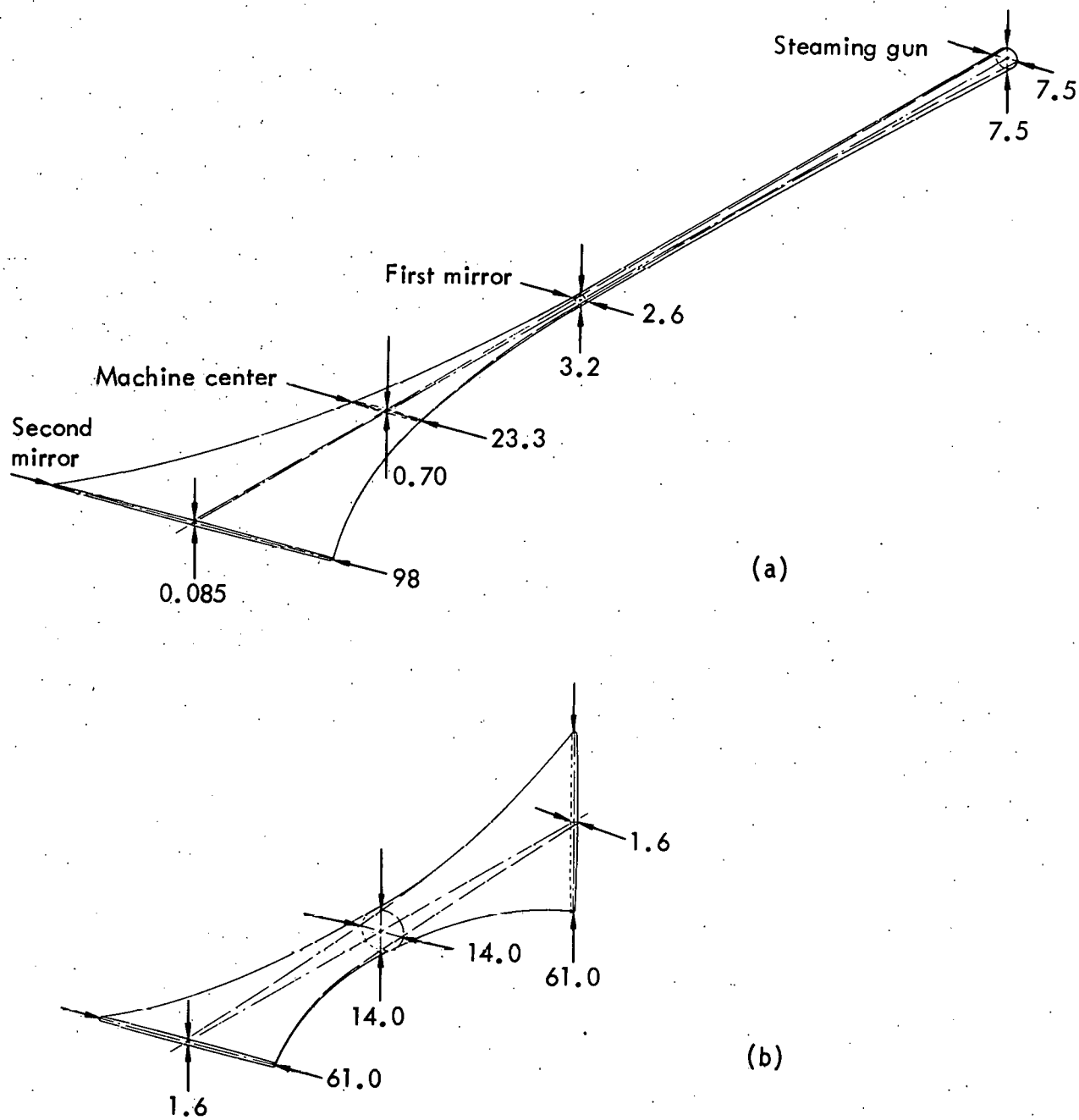

Fig. 18. Flux-tube mapping of (a) stream and (b) hot plasma. Dimensions in cm.

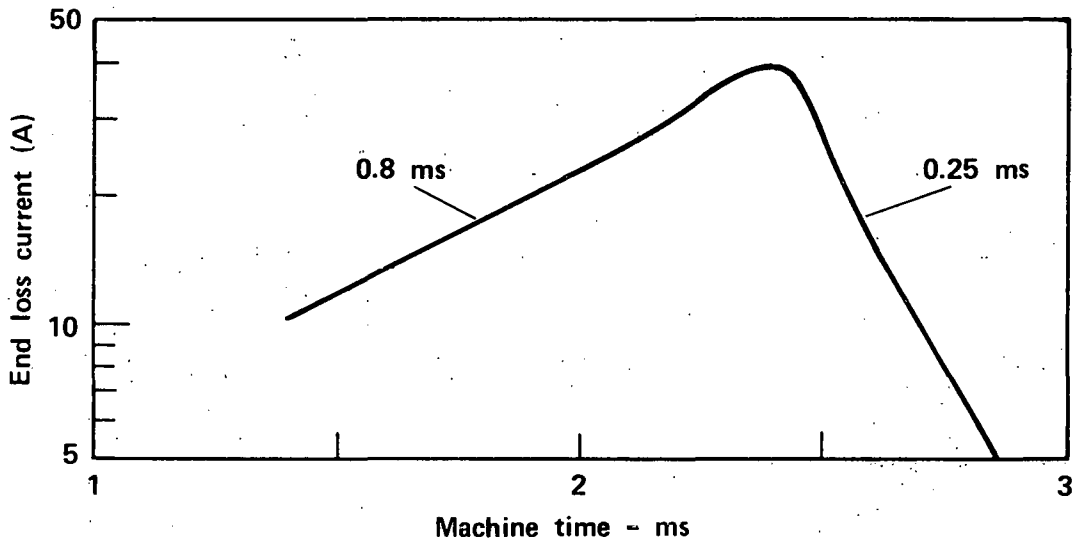

Fig. 19. End-loss current vs time.

increases with a 0.8-ms rise time and decays with a 0.25-ms time constant after beam turn-off.

The spread in end-loss ion energy is typically several hundred eV and the plasma potential is about 400 eV. From the end-loss measurement, we estimate the central density of isotropic warm plasma to be in the range of 3 to 10 $\times$ 10^{11} cm^{-3}. For a trapped density of 1 $\times$ 10^{13} cm^{-3}, this corresponds to approximately 3% to 10% of the trapped energetic density.

Vacuum Conditions

Vacuum and first-wall surface conditions can play dominant roles in determining plasma characteristics if they are not adequately controlled.[28] This section describes our methods for controlling and monitoring vacuum conditions and assessing their impact on plasma parameters. We find that high-current, long-duration, neutral beam injection results in a background-gas pressure rise that limits particle lifetimes by charge exchange.

Neutral beam injection results in charge-exchange current as high as 80 A bombarding the vacuum chamber walls. At surfaces 50 cm from the plasma, this gives a peak in wall-bombardment flux of 10^{17} atoms$\cdot cm^{-2}\cdot s^{-1}$. For the 13-keV average ion energy, the corresponding power level is 200 $W\cdot cm^{-2}$. To put the particle flux in perspective, 2XIIB fluxes are about the same as in the Fusion Engineering Research Facility (FERF) design and an order of magnitude higher than in mirror reactor designs. This wall bombardment results in a buildup of background-gas pressure that depends on the product of beam current I and the beam duration Δt, as shown in Fig. 20.

The results of a gas-flux calculation[29] are shown in Fig. 20. The curve is a best fit of the calculation to the measurements with two adjustable

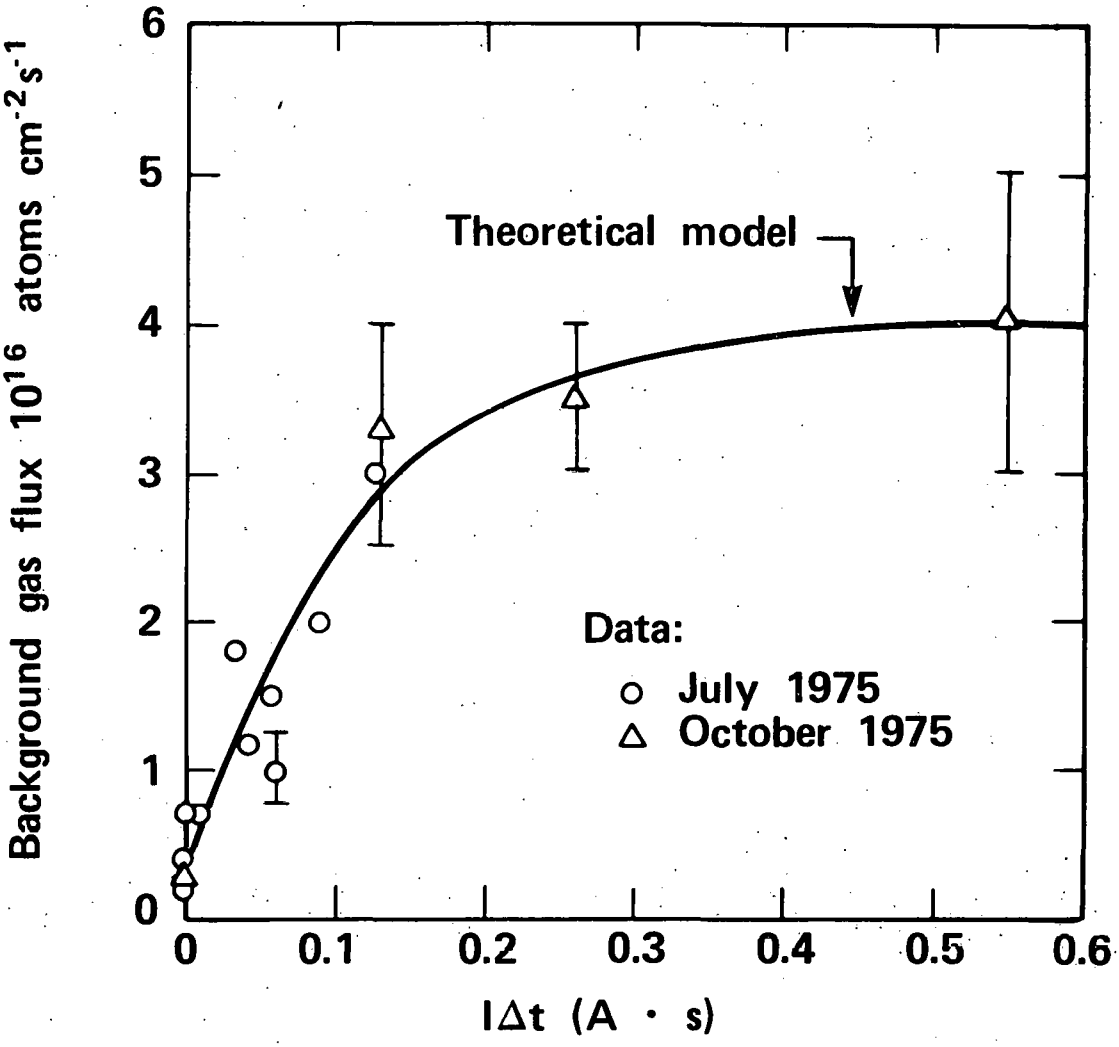

Fig. 20. Background cold-gas flux vs product of beam current and duration.

parameters: reflux coefficient and energy of desorbed species. The saturation flux level indicates that for every energetic neutral that strikes the vacuum chamber walls, 0.6 neutrals return, either by reflection or desorbtion. The buildup rate is representative of 3-eV atomic deuterium. The reflux coefficient of an ideal titanium surface is 0.15 for a typical 2XIIB ion energy distribution with a 13-keV mean ion energy. We therefore conclude that most of the background neutral flux is gas desorbed from the walls rather than reflected charge-exchange flux. In fact, in more recent experiments the reflux coefficient has been reduced to 0.3. The density decays shown in Figs. 5(a) and 6(a) when the beams shut off are both dominated by charge-exchange particle losses. Although the charge-exchange loss rate can be subtracted from the measured decay rate, this becomes imprecise when the charge-exchange rate nearly equals the density-decay rate.

An example of a shot with a 5-ms duration, high-current beam injection is shown in Fig. 21. This shot illustrates that although the plasma density can be sustained for long durations, the background gas pressure rises to $\sim 10^{17}$ atoms$\cdot$cm$^{-2}\cdot$s^{-1}. This pressure rise, due in part to gas from the neutral beam tanks, results in a rapid cooling of the mean ion energy with beam turn-off.

Background-gas charge-exchange rates can be reduced by lowering the injected beam current and duration. However, to replace the target plasma by the beam requires that $I\Delta t \geq 0.1$. This requirement is independent of density because the beam trapping efficiency is nearly proportional to density until the plasma becomes very thick. The requirement that the plasma be beam-dominated results in a charge-exchange time of 3.5 ms under the best vacuum conditions. Our longest reported lifetimes of 5 ms were corrected for a 3.5-ms charge-exchange time.

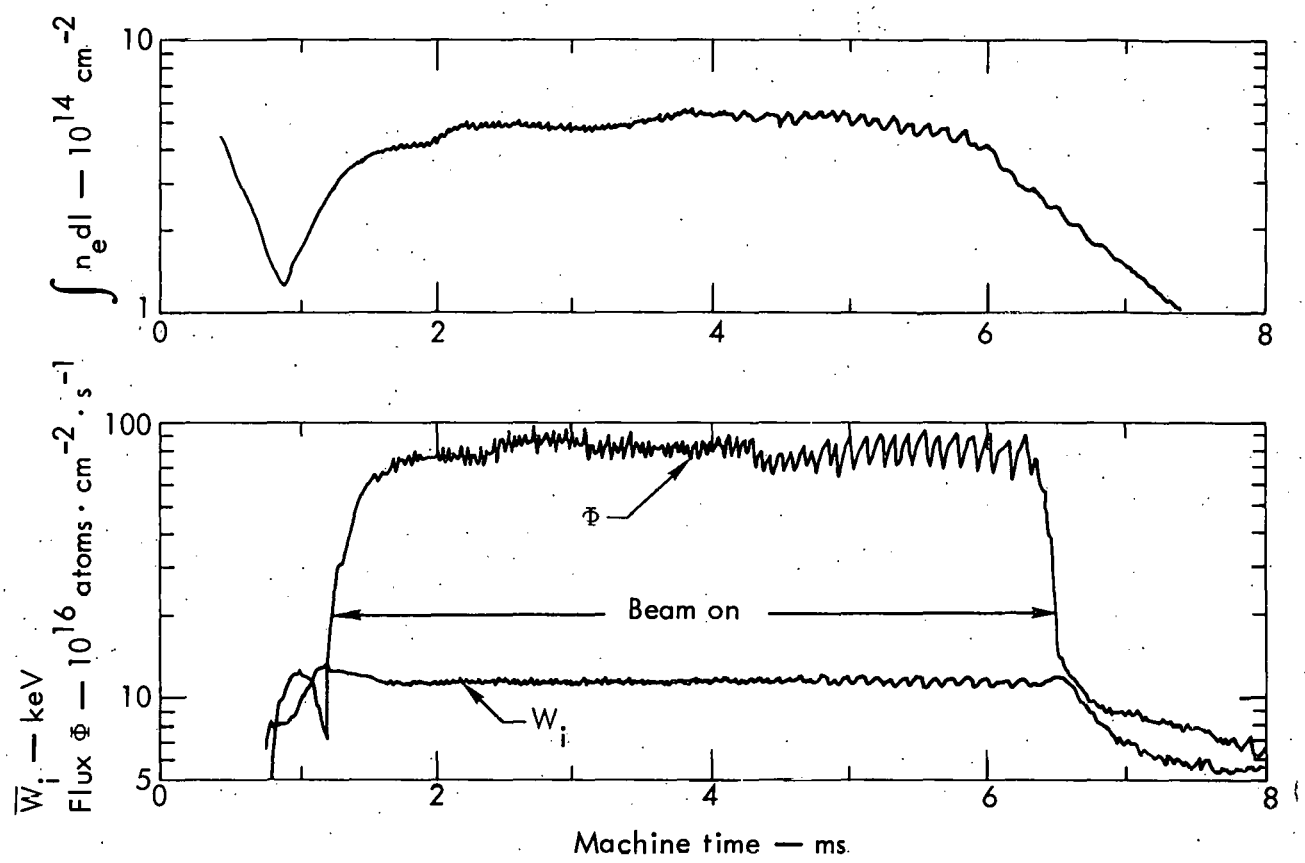

Fig. 21. Long-duration beam injection experiment.

In summary, we consider vacuum conditions to be our main technical problem. Although cold gas does not prevent buildup of hot plasmas in our present experiments, it can limit hot-ion lifetimes. We intend to reduce the amount of cold background gas by the introduction of smoother first-wall surfaces, higher-energy plasmas, and improvement in the pumping capacity of the neutral beam tanks.

ENERGY SCALING

Introduction

This section is concerned with our primary experimental objective: scaling of confinement time with ion energy. Energy density confinement time

$$\tau_{n\bar{E}} = \frac{n\bar{W}_i}{d(n\bar{W}_i)/dt} \tag{8}$$

is the most important containment time, but is difficult to measure. Only the diamagnetic loop directly measures energy density. Diamagnetic loop flux changes in 2XIIB are only a few parts in 10^3 with even the highest energy densities because the loop is wound outside the large vacuum chamber. The precision of the diamagnetic loop measurements, though adequate to confirm existence of high betas, is inadequate to determine energy density decay rates.

Diagnostics which are not so precision-limited measure either particle lifetime τ_n or ion cooling time $\tau_{\bar{E}}$,

$$\tau_n = \frac{n_i}{dn_i/dt} ,$$

and

$$\tau_{\overline{E}} = \frac{\overline{W}_i}{d\overline{W}_i/dt} .$$

The confinement times are related:

$$\frac{1}{\tau_{n\overline{E}}} = \frac{1}{\tau_n} + \frac{1}{\tau_{\overline{E}}} . \tag{9}$$

Particle loss rate and ion cooling rate are a combination of, or a balance between, a number of physical processes. For example, the particle loss rate τ_n^{-1} is the sum of (1) the Coulomb ion slowing down rate on colder electrons and the Coulomb ion-ion scattering rate into the loss cone τ_{Coul}^{-1}, (2) the charge-exchange loss on cold background gas τ_{cx}^{-1}, and (3) the turbulent diffusion rate τ_{rf}^{-1} due to ion-cyclotron fluctuations, as well as any other residual particle losses τ_0^{-1}:

$$\frac{1}{\tau_n} = \frac{1}{\tau_{Coul}} + \frac{1}{\tau_{cx}} + \frac{1}{\tau_{rf}} + \frac{1}{\tau_0} . \tag{10}$$

In low-density experiments, it is important to include particle input from the streaming plasma.

Similarly, the ion cooling rate $\tau_{\overline{E}}^{-1}$ is a competition between electron cooling and stochastic heating by plasma turbulence at the expense of particle loss.

Experimentally, our goal is to reduce and/or minimize all losses in order to maximize the net confinement time. Examples of unoptimized operation have already been discussed: Fig. 22 shows that high background-gas flux decreases the particle lifetime; and Fig. 12 shows that without the plasma stream, high-fluctuation amplitudes produce excessive turbulent plasma losses.

In the following paragraphs, we discuss three measurements of particle lifetime, each of which shows that $n\tau$ increases with ion energy. We find

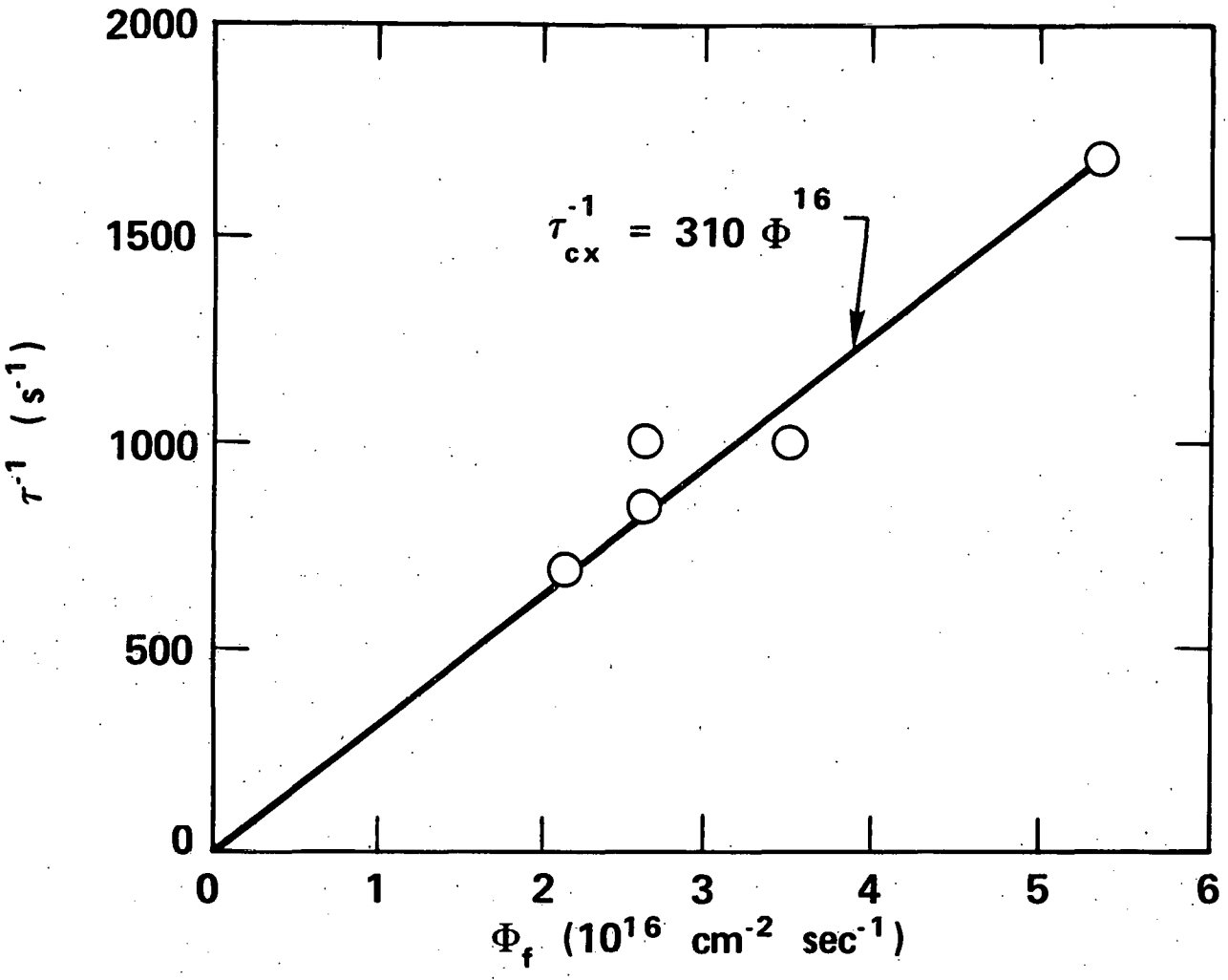

Fig. 22. Plasma loss rate vs cold-gas flux.

that the ion cooling rate follows the classical Spitzer formula and that the electron temperature slowly increases with ion energy.

Particle Lifetime

Our analysis of particle lifetime is based on the buildup equation

$$\frac{dn}{dt} = \frac{d(n_T + n_s)}{dt} = \frac{dn_T}{dt} + \frac{dn_s}{dt} =$$

$$\frac{(\overline{\sigma_i v} + \overline{\sigma_x v})}{v_b} \frac{\ell_s f_s I n_s}{eV} + \frac{\overline{\sigma_i v}}{v_b} \frac{\ell_T f_T I n_T}{eV} - \frac{n_s}{\tau_s} - \frac{n_T}{\tau_T} . \qquad (11)$$

The subscripts s and T refer to the untrapped streaming plasma and to the trapped plasma, respectively.

In Eq. (11), our notation is as follows:

n	Plasma density, cm^{-3};
σ_i and σ_x	Ionization and charge-exchange cross sections, cm^2;
v_b and v	Neutral beam and the relative particle-beam velocities, cm/s;
ℓ	Neutral beam trapping length (plasma diameter), cm;
f	Neutral beam trapping efficiency factor, averaged over the plasma density and beam current profiles;
I	Neutral beam current in equivalent amperes of deuterium atoms, A;
V	Plasma volume, cm^3;
τ_T^{-1}	Particle loss rate; and
τ_s^{-1}	Stream flow rate.

If we define α as the fraction of untrapped plasma, $\alpha = n_s/(n_T + n_s)$, and τ_{meas}^{-1} to be the measured particle buildup rate, $\tau_{meas}^{-1} = n^{-1} dn/dt$, then

$$\frac{1}{\tau_{meas}} = \frac{fI\ell}{eV} \frac{\overline{\sigma_i v} + \alpha \overline{\sigma_x v}}{v_b} - \frac{\alpha}{\tau_s} - \frac{1 - \alpha}{\tau_T} . \quad (12)$$

In Eq. (12), we have taken $\ell_s = \ell_T$ and $f_s = f_T$.

Three methods are used to determine the particle lifetime; measurement of the density decay rate after neutral beam turn-off, measurement of the initial density buildup rate with neutral beams on, and finally, measurement of the neutral beam current required to sustain the plasma at a constant density. In each of these methods, we determine density from microwave interferometer line-density measurements. In interpreting such data, we assume that the plasma diameter and the angular distribution are constant. Plasma profile measurements confirm that these are good assumptions. The particle input of the streaming plasma is represented by the term α/τ_s. Although the stream contribution is small, it is not constant in time and can introduce an observable contribution to the rate of change of density if the hot-plasma density is not well above 10^{13} cm^{-3}. In these cases, we correct for the presence of the stream.

Density Decay with Beam Turn-Off

Figure 6 shows an example of a shot where particle lifetime is measured with the neutral beams turned off. With high-current, long-duration beam injection, this shot has high plasma beta and neutron production, but particle lifetime is limited to 1 ms by charge exchange on the background gas.

A shot with reduced beam duration and therefore increased charge-exchange time (3.3 ms) is shown in Fig. 23. This low-density shot shows the effect of plasma stream on particle lifetime; notice the increased density decay rate when the stream is turned off.

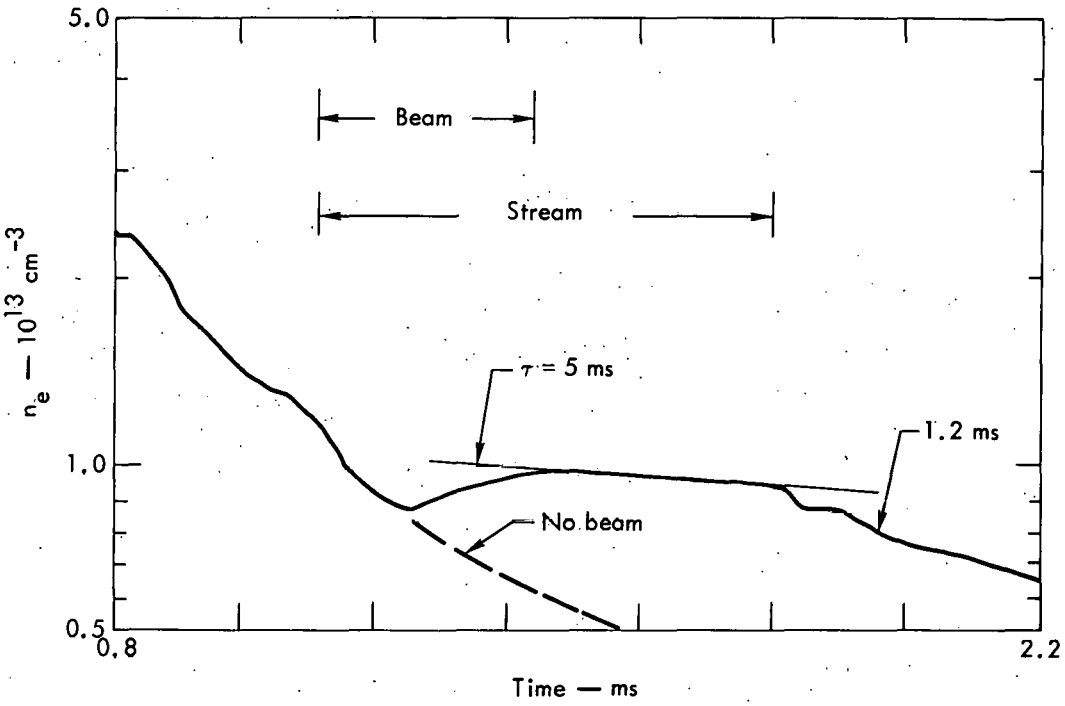

Fig. 23. Measurement of particle lifetime with beam turned off.

Based on end-loss analyzer measurements, we take 0.8 ms as the stream buildup time constant and 0.25 ms as the decay constant. By applying Eq. (12) to Fig. 23, we can solve for the fraction of warm plasma α and the particle lifetime τ_T by taking the measured time constant with stream on (τ_{meas} = -5.0 ms) and with stream off (τ_{meas} = -1.2 ms):

$$-\frac{1}{5.0} = \frac{\alpha}{0.8} - \frac{1-\alpha}{\tau_T},$$

$$-\frac{1}{1.2} = -\frac{\alpha}{0.25} - \frac{1-\alpha}{\tau_T}.$$

From the above equations, we find α = 0.12, and τ_h = 2.5 ms. Now subtracting the charge-exchange contribution τ_{cx} = 3.5 ms per Eq. (10), we find a hot-ion containment time τ = 9 ms, and $n\tau = 8 \times 10^{10}$ cm^{-3}·s. This correction is substantial and consequently has large uncertainty in the final result.

Generally, charge-exchange corrections have not been made to the data. Instead, charge-exchange-limited shots are not included in the data set used to measure particle containment times. The charge-exchange time is known accurately enough to ascertain if charge-exchange losses are important, but not accurately enough to make substantial correction to these data.

The data represented by open circles in Fig. 24 summarize the measured values of $n\tau$ vs ion energy obtained by the beam turnoff method described above. These data show $n\tau$ increasing with ion energy.

Density Buildup Rate with Beam On

The second method of determining particle lifetime uses the measurement of initial density buildup rate with neutral beam injection. Fig. 25 shows the measured rate, τ^{-1}, from microwave interferometer data vs injected beam current. These measurements are taken while ion-cyclotron fluctuations are suppressed by the stream. The zero current intercept determines the particle

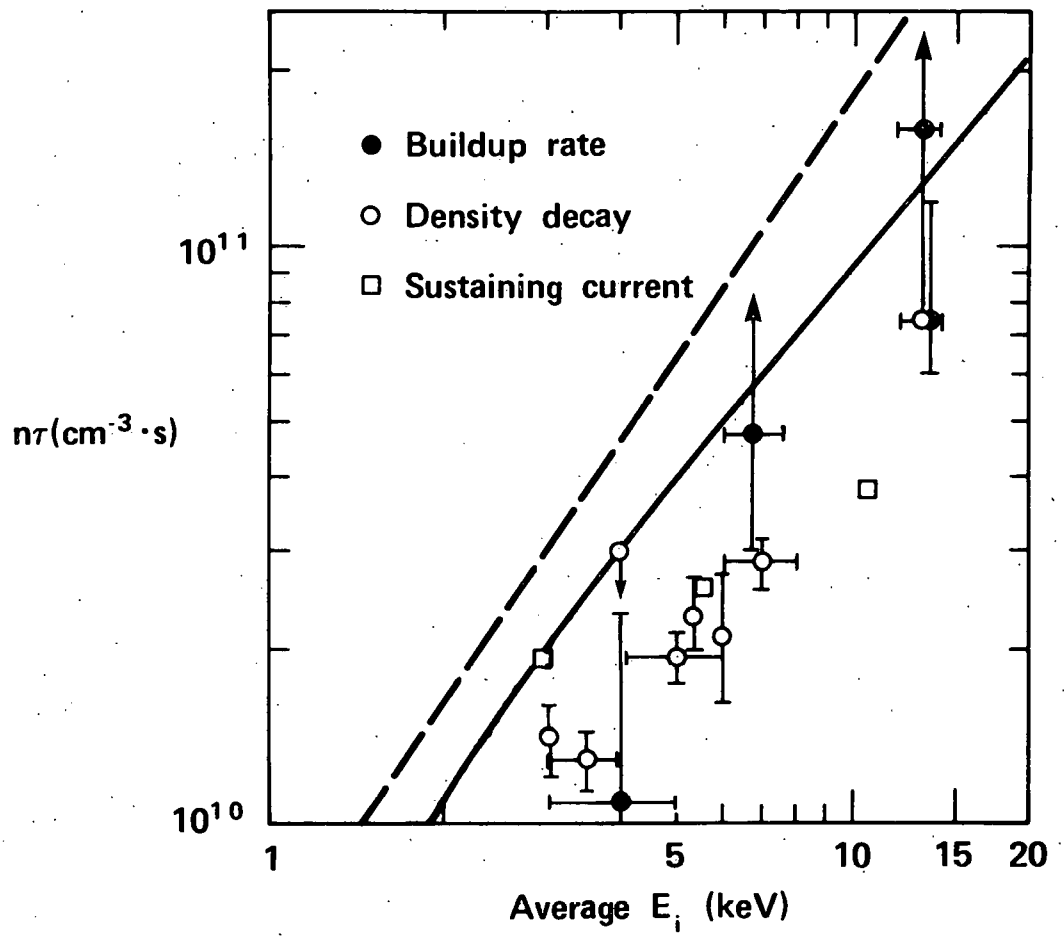

Fig. 24. Particle lifetime $n\tau$ vs ion energy. Dashed line is ion-ion scattering. Solid line includes electron drag losses.

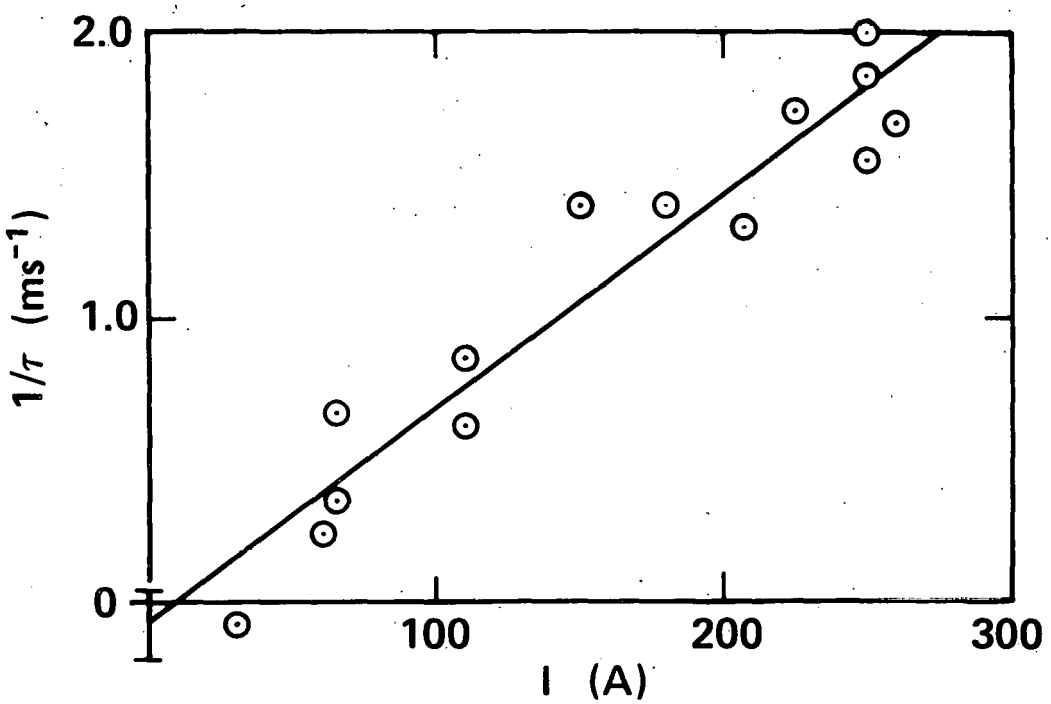

Fig. 25. Density buildup rate vs neutral beam injection current.

loss rate according to Eq. (12). This intercept corresponds to a 10-ms particle lifetime with a 5-ms lower standard deviation limit. Particle lifetime measurements at a plasma density equal to 1.5×10^{13} cm^{-3} are shown vs mean ion energy as the solid dots in Fig. 24. Again, $n\tau$ increases with ion energy, and the values obtained are consistent with the first method.

Beam Current Required to Sustain Plasma

The third method of determining particle lifetime uses the neutral beam current required to sustain the plasma at constant density. Figure 26 shows that the current required to sustain the plasma at 1.5×10^{13} cm^{-3} density decreases with increasing energy of the injected neutral beams. Again, the measurements are interpreted using Eq. (12). We take $1/\tau_{meas} = 0$, $\alpha = 0.12$, $\tau_W = 0.8$ ms, $f = 0.5$, $V = 4.5$ litres, $\ell = 14$ cm, and find

$$1/\tau_T = \frac{fI\ell}{eV} \frac{\overline{\sigma_i v} + \alpha \overline{\sigma_x v}}{v_b(1 - \alpha)} - \frac{\alpha}{1 - \alpha} \frac{1}{\tau_s} = 5.6I + 110 s^{-1} . \qquad (13)$$

Values of $n\tau$ based on this measurement are shown on Fig. 24 as squares.

Ion Cooling Rate

A few hundred microseconds after neutral beams are turned off, the mean energy of the confined ions decreases as shown in Fig. 6. Immediately after the beam switch off, the energy distribution hardens during the 0.2-ms period that the ion-cyclotron fluctuations subside. Thereafter, the mean ion energy decreases with a time constant τ_E. We have found the $n\tau_E$ scales according to the Spitzer[30] rate as shown in Fig. 27. The data of Fig. 27 have not been corrected for charge-exchange cooling or for residual stochastic heating. Both these effects are estimated to be small. The factor 5 variation in electron temperature was produced accidentally by a vacuum leak on the end

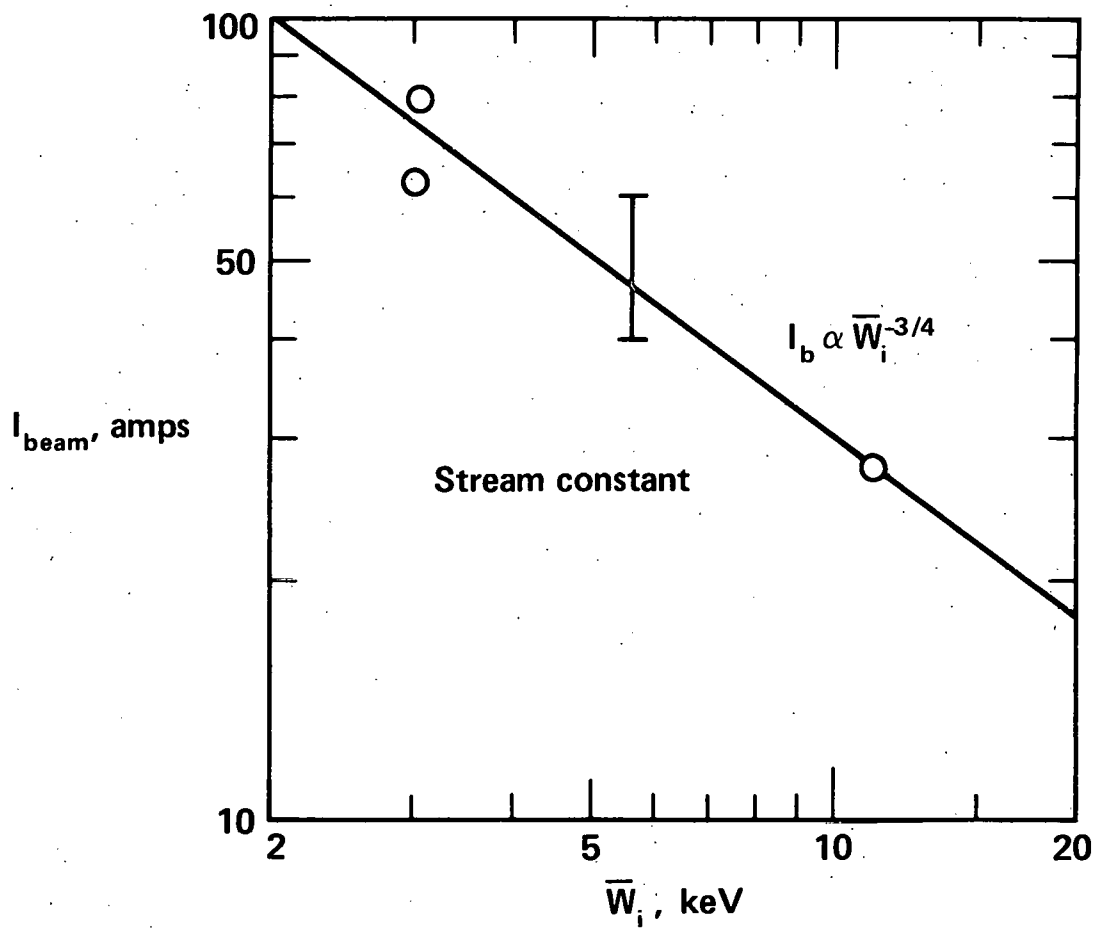

Fig. 26. Beam current required to sustain plasma at 1×10^{13} cm^{-3} density vs mean ion energy.

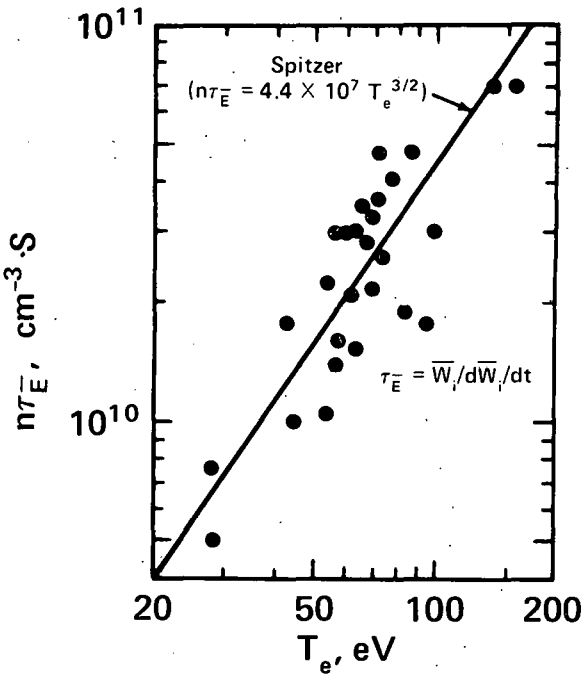

Fig. 27. Ion cooling rate vs electron temperature.

flange, which momentarily opened when the magnet was fired. This puffed air into the fans near the streaming plasma guns 3 m from the hot plasma. The gas input rapidly cooled the electrons, but did not charge exchange the hot plasma until ~3 ms later.

Electron Temperature Scaling with Ion Energy

If $n\tau$ is dominated by electron drag, then the variation of electron temperature (T_e) with ion energy (W_i) is the governing link between $n\tau$ and ion energy. The electron power balance equation[10] is

$$\frac{d}{dt}\left(\frac{3}{2} n_i T_e\right) = \frac{n_i^2 W_i \times 10^3}{4.4 \times 10^7 \, T_e^{3/2}} - n_s \nu_s \eta T_e \, , \tag{14}$$

where T_e is in eV, and W_i is in keV. The net energy lost per electron lifetime is ηT_e. Energy input from the streaming gun is neglected. The streaming plasma (n_s) cools electrons at the throughput rate

$$\nu_s \sim (3kT_e/M_i)^{1/2}/L \, , \tag{15}$$

which depends on ion sound speed and an effective plasma length. In equilibrium, we find from Eq. (14) that for deuterons

$$T_e \sim 27\left(\frac{n_i^{13} W_i L}{\eta n_s/n_i}\right)^{1/3} , \tag{16}$$

where n_i^{13} is the density in units of 10^{13} cm^{-3}.

Thus, we expect electron temperature to increase with (1) increasing ion energy density, (2) increasing plasma length, (3) decreasing stream density, and (4) decreasing electron losses. For fixed ion and stream densities, the electron temperature increases with the cube root of ion energy. Equation (16) neglects electron cooling due to cold gas.

Figure 28 shows measured electron temperature vs mean ion energy. These data are from our best vacuum conditions with ion densities between 1 to 2×10^{13} cm^{-3}. The three highest electron temperatures (at W_i = 13 keV) were obtained with less streaming plasma and qualitatively support the stream density scaling of Eq. (16).

The measured electron temperature increases slowly with ion energy, as seen in Fig. 28. The rate of increase is not well defined due to the scatter in the data. Square-root or cube-root scalings cannot be distinguished.

We have shown in Fig. 28 a line

$$T_e = 40(W_i)^{1/2} \text{ eV} \tag{17}$$

that is the upper envelope of all the measurements. The square-root dependence is suggested theoretically[10] from Eq. (16) with $n_s/n_i \propto T_e/W_i$. This line does not represent either lower-temperature measurements made under poor vacuum conditions or unoptimized stream input that are not included in the theory.

Discussion of Energy Scaling

In this section, we discuss the connection between the energy scaling measurements of particle lifetime, ion cooling rate, and electron temperature. Due to the scatter in the experimental data, we cannot expect quantitative agreement, rather we are striving for a consistent picture.

First, it is important to consider the importance of ion-ion angle scattering[31]

$$n\tau_{ii} = 2 \times 10^{10} E_i^{3/2} \log_{10} R \tag{18}$$

into the loss cones relative to electron drag into the ambipolar hole

$$n\tau_{ie} = 4.4 \times 10^{7} T_e^{3/2} \ln (E_i/E_h) \ . \tag{19}$$

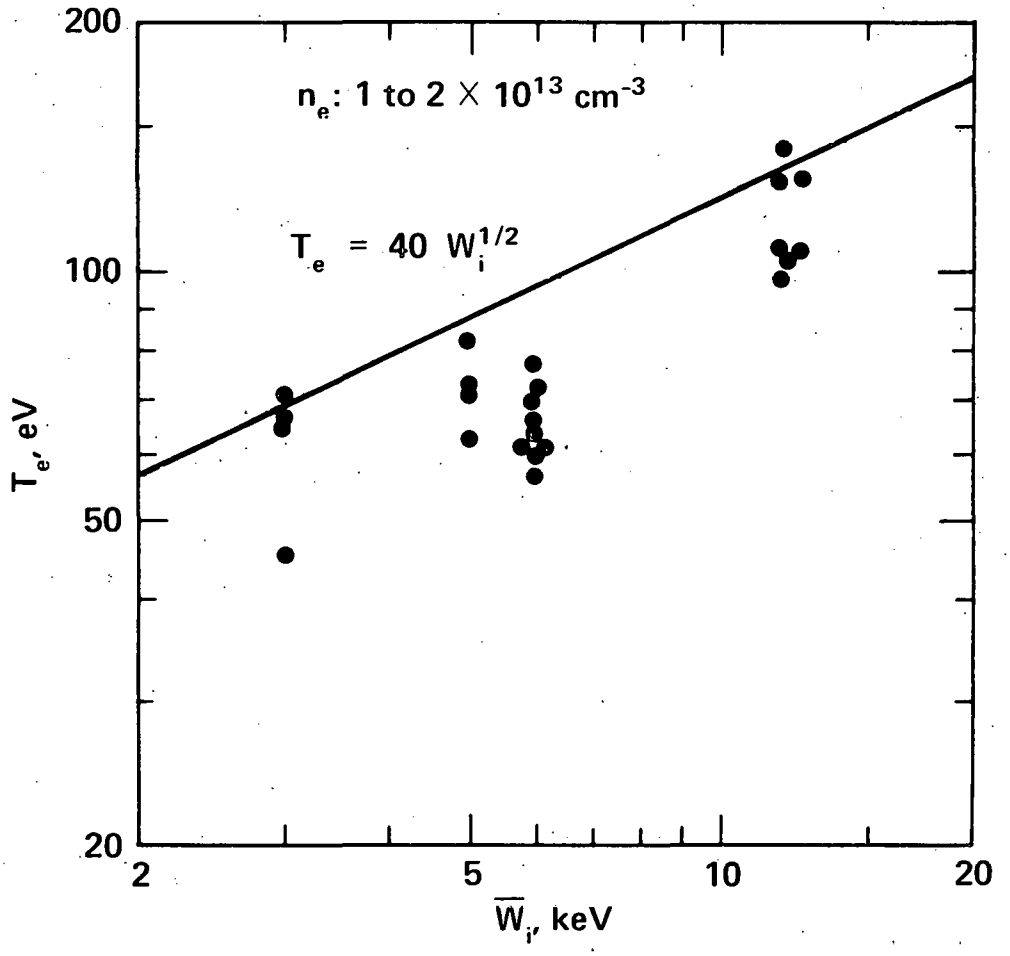

Fig. 28. Electron temperature vs ion energy.

The term $\ell n\ (E_i/E_h)$ is a measure of the "distance" to the ambipolar hole, E_h. Here, E_i and E_h are in keV, T_e is in eV, and the mirror ratio is R = 2.

Let us compare the two processes by taking $E_h = 3E_e$,

$$\frac{n\tau_{ie}}{n\tau_{ii}} = 126\left(\frac{E_e}{E_i}\right)^{3/2} \ell n\ (E_i/3E_e)\ . \tag{20}$$

Table 1 shows that this ratio is unity for $E_e/E_i = 0.02$. For the data shown in Fig. 28, $0.015 < E_e/E_i < 0.03$. Thus, 2XIIB operates in the range where electron drag and angular scattering are comparable.

Table 1. Comparison between electron drag and angular scattering time scales.

E_e/E_i	$(n\tau)_{ie}/(n\tau)_{ii}$
0.01	0.44
0.02	1.00
0.04	2.14
0.10	4.80

To estimate the combined effect of electron drag and ion-ion scattering, we calculate the sum of these two loss processes as described by Eqs. (19) and (18):

$$\frac{1}{n\tau} = \frac{1}{n\tau_{ie}} + \frac{1}{n\tau_{ii}}\ . \tag{21}$$

This estimate will overestimate $n\tau$ since it neglects turbulent wave diffusion and since it is for the maximum measured electron temperature. It does provide a simple physical model for our present discussion.

With the experimentally determined electron temperature, Eq. (17), $n\tau$ becomes

$$(n\tau)^{-1} = (5.5 \times 10^9 E_i^{3/4} \ln 31E_i)^{-1} + (6 \times 10^9 E_i^{3/2})^{-1} . \qquad (22)$$

The $n\tau$ curve calculated according to Eq. (22) is shown in Fig. 24. The slope of this curve at 10 keV indicates a $E_i^{1.2}$ scaling. For comparison, ion-ion scattering $n\tau = 6 \times 10^9 E_i^{3/2}$ is shown as the dashed curve.

We conclude that the envelope of our highest $n\tau$ data can be described, within a factor less than 2, by electron drag into the ambipolar hole and by angular ion-ion scattering.

BEAM BUILDUP ON A STREAM IN A DC MAGNETIC FIELD

Introduction

The production of a dense, energetic target plasma in a steady-state magnetic field has been a major technical problem facing the magnetic mirror program. Dense high-energy and high-beta, mirror-confined plasmas have been produced in the 2X series of experiments using fast, pulsed, magnetic mirrors for time-of-flight trapping of target plasma. As described earlier in this report, this plasma target is suitable for buildup with neutral beams if stabilized with streaming plasma. The major disadvantage of this technique is the difficulty of combining pulsed trapping fields with the steady-state superconducting magnetic fields desired in a reactor.

Previously, a number of methods for startup in steady-state magnetic fields have been suggested, but none have been demonstrated. These methods can be divided into two categories: (1) in situ creation of the target plasma, and (2) external production and injection of the target plasma. The first method attempted in category (1) was Lorentz ionization of energetic

neutrals injected into a high vacuum.[32-35] Instabilities have thus far limited the plasma density attained by this method to below 10^{10} cm^{-3}.

High-beta (0.5) plasmas have been created *in situ* by electron-cyclotron resonance breakdown and heating of a background gas.[36] However, the maximum densities obtained by this method have been limited to less than 10^{12} cm^{-3}, and there is the unsolved problem of high gas density surrounding the plasma created this way. Experiments in which a target plasma is produced by laser irradiation of a pellet are in progress,[37,38] and may produce a suitable *in situ* target plasma for buildup.

In the second category, externally produced plasmas that have been suggested as possible targets for injection into a steady-state magnetic mirror field include an arc discharge[39] and an injected plasma to be heated and trapped by electron-cyclotron resonance.[40]

This section discusses experiments that have shown that the streaming plasma used for stabilization can be injected into a quasi-steady-state magnetic field to form a target plasma. With neutral beam injection, the plasma builds up to densities and energies similar to those achieved previously with target plasmas that were trapped by pulsed magnetic fields.

Experimental Results

We approximated a steady-state magnetic field by delaying the injection of the plasma stream and neutral beams until the peak of the pulsed magnetic field. The field then decayed with an L/R time of 10 ms, so was nearly constant for the 2-ms duration of the streaming plasma.

The circular cross-section streaming plasma fans out horizontally as it moves along the minimum-B magnetic field lines, as shown in Fig. 18. This geometrical plasma shape is unstable to the interchange instability, which

probably accounts for the plasma evolving to a circular cross section in about 1 ms. The 12 neutral beams are injected within 10° of parallel to the major diameter, as shown in Fig. 29. They were aligned to cross the vertical median plane at 3 cm above and below the axis.

The plasma line density, measured across the minor diameter of the streaming plasma in the containment region, is shown in Fig. 30(a). Without neutral beam injection, the streaming plasma reaches a line density $\int ndl \approx 5 \times 10^{13}$ cm^{-2}. The ion energy is not accurately known, but is less than 1 keV.

Injecting 330 A of deuterium atoms at 13 keV, simultaneously with streaming-plasma injection, results in a buildup of line density to $\int ndl = 4.8 \times 10^{14}$ cm^{-2} within the 2-ms stream duration [Fig. 30(a)]. This line density is an order of magnitude greater than that with the stream alone, and equals the best previously achieved with the aid of a target plasma trapped by pulsed magnetic fields.

An independent measurement of the plasma density profile has been made by neutral beam attenuation through various chords of the plasma. This yields a mean diameter of 13 cm, which when combined with the above measurement of line density gives a peak density of 3.6×10^{13} cm^{-3}. The streaming-plasma density is less well known, since the stream ellipticity is not accurately measured, and the presence of hot plasma may affect the stream density.

The ion-cyclotron instability level, $\tilde{\phi}$, detected by the high-impedance probe beyond the mirror is shown in Fig. 30(b). Except for regular bursts, $\tilde{\phi}$ remains low for the 2.3-ms duration of the streaming plasma, and the plasma line density continues to increase. At 3.4 ms, the streaming plasma shuts off, and $\tilde{\phi}$ increases sufficiently to cause the plasma density to decay, even

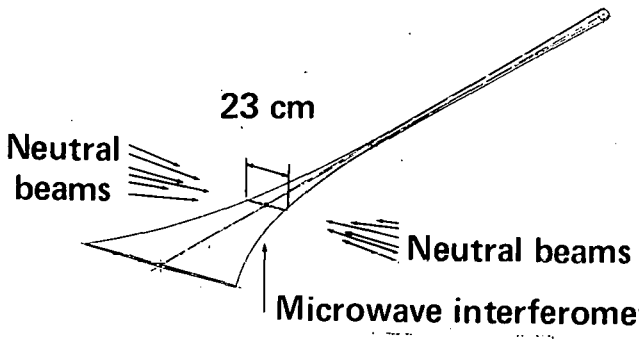

Fig. 29. Buildup and stream geometry.

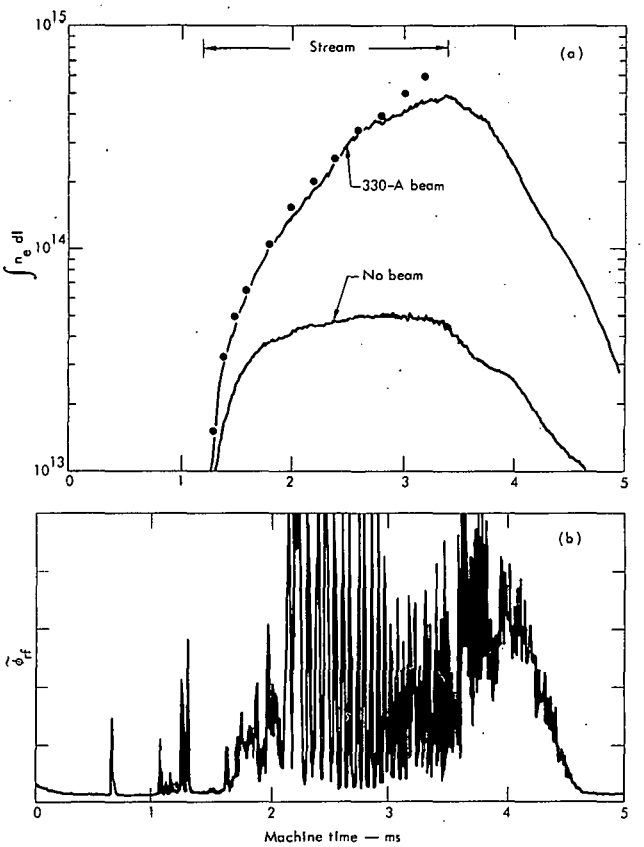

(a)

(b)

Fig. 30. Buildup on stream vs time for (a) electron line density, and (b) ion-cyclotron fluctuation amplitude.

though the neutral beam injection continues. This stabilizing effect of streaming plasma is similar to that discussed earlier.

Two variations of these experiments were tried. First, lowering the magnetic field at the gun from 0.2 T to 0.1 T reduced the buildup rate. Reducing the dc guide field further to 0.05 T prevented buildup, apparently by reducing the amount of streaming plasma penetrating the external mirror ratio, which had increased from 7:1 to 23:1. However, enough stream penetrated to stabilize and allow buildup on a target trapped by pulsed magnetic fields.

The second variation was to inject the streaming plasma from the opposite end of 2XIIB. The stream is then mapped onto a vertical ellipse, and the neutral beams inject across the minor, rather than the major diameter. In this case, buildup occurred for magnetic fields at the streaming gun, which varied from 0.05 T to 0.2 T. However, the line density buildup now measured at 13° from the major axis was not as smooth as in Fig. 30(a), possibly because of interchange instabilities tending to collapse the plasma to an equilibrium circular cross section.

Interpretation and Discussion of Experimental Results

We interpret the trapped density buildup [Fig. 30(a)] with the injected neutral beam as trapping by ionization and charge exchange on the streaming plasma, plus trapping by ionization on the trapped plasma. The trapped plasma includes a warm component from the stream and a hot component from the beam. These considerations lead to the following rate equation:

$$\frac{dn_T}{dt} = \frac{(\overline{\sigma_i v} + \overline{\sigma_x v})\, \ell_s f_s I n_s}{v_b\, eV} + \frac{\sigma_i v\, \ell_T f_T I n_T}{v_b\, eV} - \frac{n_T}{\tau} \quad . \tag{23}$$

The notation is the same as in Eq. (11). Here, we have explicitly shown the two major loss processes: charge exchange on cold background gas and electron drag rate to the ambipolar boundary E_h. Taking the loss rates to be small and treating the coefficients of n_T as adjustable parameters, we obtain the best fit to Eq. (23), shown by the dots in Fig. 30(a). From the close agreement with the data, we conclude that the functional form of Eq. (23) describes the data well. Furthermore, estimated coefficients for Eq. (23) are within a factor of 2 of the best fit values. We therefore conclude that Eq. (23) is a reasonable description of the observed buildup by neutral beam injection on the streaming plasma target.

Initially, with n_T small, the buildup proceeds linearly in time. Then as n_T increases, the buildup becomes exponential and finally saturates. Exponentiation is necessary if the hot density is to dominate and if the mean plasma ion energy is to approach a value characteristic of the beams, rather than of the target. This requires sufficient neutral beam current to overcome charge-exchange and electron drag losses.

From Eq. (23), we obtain the condition for exponentiation

$$I > \frac{v_b\, eV_T}{\overline{\sigma_i v}\, \ell_T f_T} \frac{1}{\tau_{cx}} . \tag{24}$$

Using measured values at 3.4 ms of $\tau_{cx} \approx 1$ ms, $T_e \approx 100$ eV, $V_T = 4500$ cm^3, and $f_T = 0.55$, we require from Eq. (24) that $I > 72$ A for exponentiation to continue. The 330 A of injected current exceeds this limit by a large margin. Electron drag plays a small role since the high current injection charge exchanges away plasma ions before they cool down.

The average ion energy is 12 keV. This value is supported by the magnitude of the D-D neutron production. At the peak density of 3.6×10^{13}, the magnetic field has decayed from 0.68 to 0.56 T. From this, we infer a beta of 0.5, corrected for an estimated 10% warm-plasma density.

Advantages of this washer-type gun for startup of a neutral-beam-sustained plasma in a steady-state magnetic field include:

- Simple and inexpensive equipment is used.
- Target plasmas of arbitrary cross section can be produced with multiple guns.
- Gas efficiency of streaming plasma production is high. Most of the gas surrounding the plasma originates from charge-exchange particles bombarding the walls.
- The electron temperature is high, so electron drag times for ion energy loss are greater than 1 ms.
- The same plasma that provides the target also stabilizes ion-cyclotron instabilities.

SUMMARY AND CONCLUSIONS

This report has described the status of 2XIIB neutral beam injection experiments with a stabilizing plasma stream. The most important result is that ion-cyclotron fluctuations have been suppressed with a streaming plasma flowing along magnetic field lines. With the reduced fluctuation level, neutral beam injection has increased the plasma density to 5×10^{13} cm^{-3}. At the 13-keV ion energy, this corresponds to peak plasma betas of 0.5.

Variation of neutral beam injection energy permits us to conclude that particle lifetimes increase with mean energy of the plasma ions. The

envelope of $n\tau$ measurements reaches that calculated on the basis of electron drag and ion-ion scattering.

Warm plasma has been injected along field lines into a quasi-steady-state magnetic mirror in the 2XIIB experiment. This has provided a suitable target plasma for density buildup and heating with neutral beam injection. With the injection of 330-A equivalent of 13-keV deuterium atoms, the density exponentiated to 3.5×10^{13} cm^{-3}, the average ion energy increased to 12 keV, and the beta to 0.5.

In this report, we have used simple physical models to discuss experimental results. A quasilinear theory and a simulation code have been developed which explain, in considerable detail, most features of the experiment. These comparisons are discussed in a theoretical group report.[41]

REFERENCES

1. F. H. Coensgen, W. F. Cummins, A. W. Molvik, W. E. Nexsen, Jr., T. C. Simonen, and B. W. Stallard, in Proc. Fifth Conf. Plasma Physics and Controlled Nuclear Fusion, Tokyo, 1974 (IAEA, 1974), p. 323.
2. R. F. Post and M. N. Rosenbluth, Phys. Fluids 9, 730 (1966).
3. D. E. Baldwin, C. O. Beasley, Jr., H. L. Berk, W. M. Farr, R. C. Harding, J. E. McCune, L. D. Pearlstein, and A. Sen, in Proc. Fourth Int. Conf. Plasma Physics and Controlled Nuclear Fusion, Madison, WI, 1971 (IAEA, 1971), Vol. II, p. 735.
4. T. C. Simonen, Identification of an Ion Cyclotron Instability in a Mirror-Confined Plasma, Lawrence Livermore Laboratory Rept. UCRL-76115, Rev. I (1975); submitted to Phys. Fluids.
5. D. E. Baldwin and J. D. Callen, Phys. Rev. Lett. 28, 1686 (1972).

6. H. L. Berk, L. D. Pearlstein, J. D. Callen, C. W. Horton, and M. N. Rosenbluth, Phys. Rev. Lett. 22, 876 (1969).

7. R. F. Post, in Proc. Int. Conf. Plasma Confined in Open-Ended Geometry, Gatlinburg, TN, 1967 (ORNL, 1967).

8. Yu. V. Gott, M. S. Ioffe, B. I. Kanaev, A. G. Motlick, V. P. Pastukhov, and R. I. Subolev, in Proc. Fifth Conf. Plasma Physics and Controlled Nuclear Fusion, Tokyo, 1974 (IAEA, 1975), Vol. I, p. 341.

9. Yu. T. Baiborodov, M. S. Ioffe, B. I. Kanaev, R. I. Subolev, and E. E. Yushmanov, in Proc. Fourth Conf. on Plasma Physics and Controlled Nuclear Fusion, Madison, WI, 1971 (IAEA, 1971), Vol. II, p. 647.

10. D. E. Baldwin, H. L. Berk, and L. D. Pearlstein, Turbulent Lifetimes in Mirror Machines, Lawrence Livermore Laboratory Rept. UCRL-77641 (1976); submitted to Phys. Rev. Lett.

11. F. H. Coensgen, W. F. Cummins, B. G. Logan, A. W. Molvik, W. E. Nexsen, T. C. Simonen, B. W. Stallard, and W. C. Turner, Phys. Rev. Lett. 35, 1501 (1975).

12. T. C. Simonen, B. G. Logan, and C. Gormezano, Bull. Am. Phys. Soc. 20, 1231 (1975).

13. B. W. Stallard, W. F. Cummins, A. W. Molvik, W. E. Nexsen, T. C. Simonen, and W. C. Turner, Bull. Am. Phys. Soc. 20, 1231 (1975).

14. W. C. Turner, W. F. Cummins, W. E. Nexsen, E. J. Powers, T. C. Simonen, and B. W. Stallard, Bull. Am. Phys. Soc. 20, 1232 (1975).

15. R. H. Bulmer, M. O. Calderon, S. M. Hibbs, and T. A. Kozman, in Proc. Sixth Symp. Engineering Problems of Fusion Research, San Diego, CA, 1975 (in press).

16. S. M. Hibbs and M. O. Calderon, in Proc. Sixth Symp. Engineering Problems of Fusion Research, San Diego, CA, 1975 (in press).

17. S. M. Hibbs, in Proc. Sixth Symp. Engineering Problems of Fusion Research, San Diego, CA, 1975 (in press).

18. W. R. Baker, K. H. Berkner, W. S. Cooper, K. W. Ehlers, W. B. Kunkel, R. V. Pyle, and J. W. Stearns, in Proc. Fifth Conf. Plasma Physics and Controlled Nuclear Fusion, Tokyo, 1974 (IAEA, 1974).

19. K. H. Berkner, R. V. Pyle, and J. W. Stearns, Nucl. Fusion 15, 249 (1974).

20. W. C. Turner, A. W. Molvik, and J. Williams, "Beam Probe Measurements of Plasma Density Profiles in 2XIIB," in Proc. Topical Conf. Diagnostics of High Temperature Plasmas, Knoxville, TN, 1976 (APS, in press).

21. W. E. Nexsen, B. G. Logan, F. H. Coensgen, A. W. Molvik, and W. F. Cummins, Bull. Am. Phys. Soc. 20, 1232 (1975).

22. E. J. Powers, Phys. Fluids 16, 1374 (1973).

23. B. G. Logan, "Subkilovolt X-Ray Spectrometer for 2XIIB Employing Filters and Photocathodes," in Proc. Topical Conf. Diagnostics of High Temperature Plasmas, Knoxville, TN, 1976 (APS, in press).

24. L. S. Hall and T. C. Simonen, Phys. Fluids 17, 1014 (1974).

25. E. J. Powers and T. C. Simonen, Microwave Measurement of Plasma Density Fluctuation Amplitudes, Lawrence Livermore Laboratory Rept. UCRL-77788 (1975); submitted to J. Appl. Phys.

26. F. H. Coensgen, W. F. Cummins, and A. E. Sherman, Phys. Fluids 2, 350 (1959).

27. J. F. Steinhaus, N. L. Oleson, and W. L. Barr, Phys. Fluids 8, 1720 (1965).

28. T. C. Simonen, R. H. Bulmer, F. H. Coensgen, W. F. Cummins, C. Gormezano, B. G. Logan, A. W. Molvik, W. E. Nexsen, W. C. Turner, B. W. Stallard, G. E. Vogtlin, and R. R. Vandervoort, "Control of First-Wall Surface Conditions in the 2XIIB Magnetic Mirror Plasma

Confinement Experiment," in Proc. Conf. on Surface Effects in Controlled Fusion Devices, San Francisco, CA, 1976.

29. B. W. Stallard, Radial Plasma Buildup Code for Neutral Beam Injection into a Mirror Machine, Lawrence Livermore Laboratory Rept. UCRL-51784 (1975).

30. L. Spitzer, Physics of Fully Ionized Gases (J. Wiley, NY, 1962), 2nd ed.

31. A. H. Futch, Jr., J. P. Holdren, J. Killeen, and A. A. Mirin, Plasma Phys. 14, 211 (1972).

32. R. J. Colchin, J. L. Dunlap, and H. Postma, Phys. Fluids 13, 501 (1970).

33. E. Thompson, J. G. Cordey, and D. R. Sweetman, in Proc. Fourth Int. Conf. on Plasma Physics and Controlled Nuclear Fusion, Madison, WI, 1971 (IAEA, 1971), p. 659.

34. O. A. Anderson, D. H. Birdsall, C. C. Damm, J. H. Foote, A. H. Futch, R. K. Goodman, F. J. Gordon, G. W. Hamilton, E. B. Hooper, A. L. Hunt, J. E. Osher, and G. D. Porter, in Proc. Fifth Conf. Plasma Physics and Controlled Nuclear Fusion, Tokyo, 1974 (IAEA, 1975), Vol. I, p. 379.

35. V. A. Zhiemtsov, V. Kh. Likhtenshtezn, D. A. Panov, P. M. Kocarev, V. A. Chuyanov, and A. G. Shcherbakov, in Proc. Fifth Conf. Plasma Physics and Controlled Nuclear Fusion, Tokyo, 1974 (IAEA, 1975), Vol. I, p. 355.

36. W. B. Ard, R. A. Blanken, R. J. Colchin, J. L. Dunlop, G. E. Guest, G. R. Haste, C. L. Hedrick, N. L. Lozen, J. F. Lyon, and D. J. Sigmor, in Proc. Fourth Conf. on Plasma Physics and Controlled Nuclear Fusion, Madison, WI, 1971 (IAEA, 1971), Vol. II, p. 619.

37. A. F. Haught, W. B. Ard, W. J. Fader, R. A. Jong, A. E. Mensing, B. H. Polk, R. G. Tomlinson, and J. T. Woo, in Proc. Fifth Conf. Plasma Physics and Controlled Nuclear Fusion, Tokyo, 1974 (IAEA, 1974), p. 391.

38. J. E. Osher and G. D. Porter, Bull. Am. Phys. Soc. 20, 1238 (1975).

39. E. B. Hooper, Jr., O. A. Anderson, and D. H. Birdsall, Dense Discharge Plasma for Neutral Target in Minimum-B Mirrors, Lawrence Livermore Laboratory Rept. UCRL-76703 (1975).

40. R. Bardet, P. Briand, L. Dupas, C. Gormezano, and G. Melin, Nucl. Fusion 15, 865 (1975).

41. D. E. Baldwin, et al., Present Status of Mirror Stability Theory, Lawrence Livermore Laboratory Rept. UCID-17038 (1976).

DISTRIBUTION

External:

Senior Review Panel

Dr. Robert W. Bussard
462 Santa Cecelia
Solona Beach, California 92075

Stephen O. Dean, Chairman
Division of Controlled
Thermonuclear Research
U.S. Energy Research and
Development Administration
Washington, D.C. 20545

Dr. Harold Forsen
Exxon Nuclear Co., Inc.
777-106th Avenue, NW.
Bellevue, Washington 98004

Dr. Art Fraas
Oak Ridge National Laboratory
P. O. Box Y
Oak Ridge, Tennessee 37830

Nelson J. Grace
Division of Controlled
Thermonuclear Research
U.S. Energy Research and
Development Administration
Washington, D.C. 20545

Bennett Miller
Division of Controlled
Thermonuclear Research
U.S. Energy Research and
Development Administration
Washington, D.C. 20545

Dr. Marshall N. Rosenbluth
Institute for Advanced Study
Olden Lane
Princeton, New Jersey 08540

Dr. Alvin W. Trivelpiece
Department of Physics
and Astronomy
University of Maryland
College Park, Maryland 20742

James M. Williams
Division of Controlled
Thermonuclear Research
U.S. Energy Research and
Development Administration
Washington, D.C. 20545

Special Consultants to the Panel

Dr. Solomon J. Buchsbaum
Executive Director
Research Communications Science Div.
Bell Laboratories, Craneford Corner
Holmdel, New Jersey 07733

Dr. Tihiro Ohkawa
General Atomic Company
P.O. Box 81608
San Diego, California 92138

Technical Advisors to the Panel

Dr. Richard Aamodt
Science Applications Inc.
934 Pearl Street
Boulder, Colorado 80302

Dr. Robert Conn
University of Wisconsin
Madison, Wisconsin 53706

Dr. Ronald C. Davidson
Department of Physics
and Astronomy
University of Maryland
College Park, Maryland 20742

Dr. William Ellis
Los Alamos Scientific Laboratory
P.O. Box 1663
Los Alamos, New Mexico 87545

Dr. Gareth E. Guest
General Atomic Company
P.O. Box 81608
San Diego, California 92138

Technical Advisors, con't.

Dr. Carl Henning
Division of Controlled
Thermonuclear Research
U.S. Energy Research and
Development Administration
Washington, D.C. 20545

Dr. Terry Kammash
Nuclear Engineering Dept.
University of Michigan
Ann Arbor, Michigan 48105

Dr. Gerald Kulcinski
Department of Nuclear
Engineering
University of Wisconsin
Madison, Wisconsin 53706

Dr. Norman H. Lazar
Oak Ridge National Laboratory
P.O. Box Y
Oak Ridge, Tennessee 37830

Dr. Larry M. Lidsky
Department of Nuclear
Engineering
Massachusetts Institute
of Technology
Cambridge, Massachusetts 02139

Dr. Dale Meade
Plasma Physics Laboratory
Princeton University
P.O. Box 451
Princeton, New Jersey 08540

Dr. George Miley
Nuclear Engineering Department
University of Illinois
Champagne, Illinois 61803

Dr. F. Robert Scott
Electric Power Research Inst.
3412 Hillview Avenue
P.O. Box 10412
Palo Alto, California 94303

Dr. Don Steiner
Oak Ridge National Laboratory
P.O. Box Y
Oak Ridge, Tennessee 37830

Dr. Ravindra Sudan
Laboratory of Plasma Studies
Cornell University
Ithaca, New York 14850

Dr. Keith I. Thomassen
Los Alamos Scientific Laboratory
P.O. Box 1663
Los Alamos, New Mexico 87545

United Technologies Research Center

Dr. Alan F. Haught
United Technologies Research Center
400 Main Street
East Hartford, Connecticut 06108

Dr. Russell Meyerand
United Technologies Research Center
400 Main Street
East Hartford, Connecticut 06108

SAN Operations Office

Dr. Edward Temple
San Francisco Operations Office
1333 Broadway, Wells Fargo Building
Oakland, California 94612

Dr. Robert D. Thorne
San Francisco Operations Office
1333 Broadway, Wells Fargo Building
Oakland, California 94612

DCTR Staff Coordinators

Dr. Franklin E. Coffman
Division of Controlled
Thermonuclear Research
U.S. Energy Research and
Development Administration
Washington, D.C. 20545

Dr. Milton D. Johnson
Division of Controlled
Thermonuclear Research
U.S. Energy Research and
Development Administration
Washington, D.C. 20545

DCTR, con't.

Dr. Edwin E. Kintner
Division of Controlled
Thermonuclear Research
U.S. Energy Research and
Development Administration
Washington, D.C. 20545

Dr. Oscar P. Manley
Division of Controlled
Thermonuclear Research
U.S. Energy Research and
Development Administation
Washington, D.C. 20545

PPPL

Dr. Melvin B. Gottlieb
Princeton Plasma Physics Laboratory
Princeton University
P.O. Box 451
Princeton, New Jersey 08540

Oak Ridge

Dr. John F. Clarke
Oak Ridge National Laboratory
P.O. Box Y
Oak Ridge, Tennessee 37830

LASL

Dr. Fred L. Ribe
Los Alamos Scientific Laboratory
P.O. Box 1663
Los Alamos, New Mexico 87545

Assistant Administrator for
Solar, Geothermal, and Advanced
Energy Systems

Dr. Robert L. Hirsch
Division of Controlled
Thermonuclear Research
U.S. Energy Research and
Development Administration
Washington, D.C. 20545

Internal:

D. E. Baldwin	L-388
R. E. Batzel	L-1
H. L. Berk	L-388
J. A. Byers	L-388
J. F. Clauser	L-386
F. H. Coensgen (50)	L-382
R. H. Cohen	L-388
D. L. Correll	L-387
W. F. Cummins	L-386
T. A. Cutler	L-388
T. K. Fowler (8)	L-382
C. Gormezano	L-386
M. A. Harrison (50)	L-382
G. B. Logan	L-386
N. Maron	L-382
A. W. Molvik	L-386
M. L. Nelson (10)	L-382
W. E. Nexsen	L-386
L. D. Pearlstein	L-388
R. F. Post	L-386
M. E. Rensink	L-388
T. D. Rognlien	L-388
T. C. Simonen	L-386
B. W. Stallard	L-386
J. J. Stewart	L-388
C. E. Taylor	L-386
W. C. Turner	L-386
D. C. Watson	L-388
CTR LIBRARY	L-387
TIC Oak Ridge (27)	
TID (15)	L-9

NOTICE

"This report was prepared as an account of work sponsored by the United States Government. Neither the United States nor the United States Energy Research & Development Administration, nor any of their employees, nor any of their contractors, subcontractors, or their employees, makes any warranty, express or implied, or assumes any legal liability or responsibility for the accuracy, completeness or usefulness of any information, apparatus, product or process disclosed, or represents that its use would not infringe privately-owned rights."

Printed in the United States of America
Available from
National Technical Information Service
U. S. Department of Commerce
5285 Port Royal Road
Springfield, Virginia 22151
Price: Printed Copy $___*; Microfiche $2.25

*Pages	NTIS Selling Price
1-50	$4.00
51-150	$5.45
151-325	$7.60
326-500	$10.60
501-1000	$13.60

Technical Information Department
LAWRENCE LIVERMORE LABORATORY
University of California | Livermore, California | 94550